GEOPERSIA

Accepted Manuscript

Application of ASTER Sensor Data for Industrial Mineral Mapping: A Case Study of the Semirom Kaolin Deposit, Zagros Orogenic Belt, Iran

Reza Khaledi, Shojaeddin Niroomand, Abdorrahman Rajabi

DOI: 10.22059/geope.2025.396189.648825

Receive Date: 27 May 2025
Revise Date: 23 October 2025
Accept Date: 07 June 2026

Application of ASTER Sensor Data for Industrial Mineral Mapping: A Case Study of the Semirom Kaolin Deposit, Zagros Orogenic Belt, Iran

Reza Khaledi, Shojaeddin Niroomand *, Abdorrahman Rajabi

School of Geology, College of Science, University of Tehran, Tehran 1417935840, Iran

Received: 27 May 2025, Revised: 23 October 2025, Accepted: 07 June 2026

Abstract
Accurate mineral mapping in structurally complex terrains is essential for effective resource exploration. This study investigates the application of ASTER satellite imagery integrated with spectral processing techniques and supervised machine learning algorithms to identify key industrial minerals in the Semirom kaolin deposit, located in the Zagros fold-and-thrust belt, Iran. Methods applied include Band Ratio (BR), Relative Band Depth (RBD), spectral indices, Principal Component Analysis (PCA), Directed PCA (DPCA), Band Ratio Color Composite (BRCC), Random Forest (RF), and Support Vector Machine (SVM). Field surveys and X-ray diffraction (XRD) analyses were used for ground validation. Kaolinite-rich horizons were reliably delineated using the Kaolinite Index (KLI), PCA, DPCA, and both machine learning classifiers, with SVM achieving an overall accuracy of 77.2% (Kappa = 0.67) and outperforming RF (69.1%, Kappa = 0.55). Calcite was best detected using DPCA applied to SWIR bands in combination with the Calcite Index (CLI), while hematite was only partially discriminated in mixed-pixel zones through BR and SVM classification. Major limitations included spectral overlaps between minerals, erosional cover, and mixed-pixel effects caused by heterogeneous surface conditions. The results highlight the potential of integrating ASTER data with advanced image processing and machine learning as a cost-effective and reliable framework for preliminary exploration of clay-rich deposits. Furthermore, kaolinitic horizons at the Ilam–Sarvak boundary coincide with known bauxite occurrences.

Keywords: ASTER, Mineral Mapping, Machine Learning, Kaolin Deposit, Zagros Orogenic Belt.

Introduction

Kaolin represents a significant group of 1:1 layered phyllosilicate minerals within the tetrahedral–octahedral sheet structure. This group encompasses several polymorphs of similar chemical composition but distinct crystallographic arrangements, including kaolinite ($Al_2Si_2O_5(OH)_4$), dickite ($Al_2Si_2O_5(OH)_4$), nacrite ($Al_2Si_2O_5(OH)_4$), and the hydrated form halloysite ($Al_2Si_2O_5(OH)_4 \cdot 2H_2O$). The subtle structural differences among these polymorphs strongly influence their physical properties, industrial applications, and geological occurrence, rendering kaolin deposits an important target in both economic geology and resource exploration. These minerals typically form through processes such as chemical weathering, hydrothermal alteration, or sedimentary deposition of parent rocks including granite, rhyolite, and volcanic tuffs. Owing to its white color, softness, and distinctive physicochemical properties, kaolin is widely utilized in the ceramics, paper, paint, plastics, rubber, fiberglass, and cement industries. Specific varieties have specialized applications: bauxitic kaolin in

* Corresponding author e-mail: niroomand@ut.ac.ir

refractories, micaceous kaolin in ceramics, and dispersible types in pigments. The economic significance of kaolin is largely determined by its purity, textural characteristics (e.g., hardness, dispersibility, plasticity), and extraction techniques (Ece & Ercan, 2024).

In Iran, karst-type bauxite deposits, enriched in alumina (Al_2O_3), titania (TiO_2), and high-field-strength-element (HFSE)-bearing minerals such as zircon ($ZrSiO_4$), tourmaline ($Na(Mg,Fe)_3Al_6(BO_3)_3Si_6O_{18}(OH)_4$), and rutile ($TiO_2$), are distributed across four major regions: (1) the Sanandaj-Sirjan Zone, with Permo-Triassic and Late Triassic deposits in Bukan and Kanshiteh; (2) the Zagros Fold Belt, hosting Upper Cretaceous and Triassic occurrences in Mandan, Deh-now, Sarfaryab, and Dopolan; (3) the Alborz Mountains, containing Upper Triassic deposits in Tilabad and Jajarm; and (4) the Central Iranian Plateau, with Upper Triassic and Permo-Triassic deposits in Bazargan and Balbaloyeye. These deposits developed under hot and humid Phanerozoic climatic conditions through intense weathering of carbonate rocks and subsequent karstification. The Semirom kaolinite-bauxite deposit in Isfahan Province shares a geological affinity with these karst-type bauxites; however, due to inadequate conditions for complete bauxitization, it is characterized by limited bauxite horizons and extensive kaolin layers, which form the primary ore. Owing to its refractory characteristics, this deposit represents one of the key refractory raw material sources in Iran (Khaledi, 2022).

Despite the abundance of kaolinite-bauxite deposits in the Zagros region and their close geological affinities, the application of remote sensing techniques for their detection has remained limited. The present study applies remote sensing methods to identify previously unrecognized kaolin deposits.

The identification and classification of mineralogical features at various scales represent a critical endeavor in both geological studies and mineral exploration. Over the past two decades, significant advancements in satellite remote sensing technologies, particularly the Advanced Spaceborne Thermal Emission and Reflection Radiometer (ASTER) sensor aboard the TERRA satellite, have considerably enhanced the ability to achieve this objective. ASTER's superior spatial resolution and spectral capabilities provide high-quality datasets that are indispensable for geological investigations (Shebl et al., 2023; Sikakwe, 2023).

While primary rock-forming minerals such as quartz (SiO_2) and feldspar ($(K,Na,Ca)(Al,Si)_4O_8$) exhibit minimal absorption features in the visible and near-infrared (VNIR) and Shortwave Infrared (SWIR) ranges, they present significant molecular absorption characteristics in the thermal infrared (TIR) range. This, coupled with the high spectral and spatial resolution of ASTER, makes it an invaluable tool for mapping silicate and carbonate rock formations, volcanic studies, urban environmental analysis, lithological mapping, and coastal ecosystem monitoring (Mohamed et al., 2021).

The ongoing development of advanced ASTER data processing methodologies for the identification of carbonate, silicate, and mafic rock units is a pivotal aspect of geological remote sensing. Furthermore, the enhanced delineation of clay minerals, particularly kaolinite, which serves as a key indicator of argillic alteration, is of paramount importance for exploring metallic mineral deposits (Esmaeilzadeh et al., 2023; Abdelkareem et al., 2024; Habashi et al., 2024; Hajaj et al., 2024; Islam et al., 2024).

Recent studies have demonstrated that remote sensing data plays a significant role in the identification and delineation of non-metallic mineral deposits and industrial clays such as kaolinite, bentonite, phosphate, talc, and gypsum (Shuai et al., 2022; Canbaz & Karaman, 2024; Jain & Bhu, 2024). These findings indicate that remotely sensed information can be effectively used to pinpoint mineralized zones, prioritize exploration targets, and reduce the cost of field-based investigations. This knowledge is particularly valuable in regions with limited accessibility or sparse geological data, where it serves as a strategic tool during early-stage exploration and supports more informed technical and economic decision-making. The growing application of remote sensing in geological investigations (particularly in the exploration of industrial clay deposits such as kaolin) highlights the need to assess and compare different spectral processing techniques in order to identify the most effective approach for future studies. This study explores the potential of ASTER satellite imagery combined with advanced spectral analysis techniques for detailed mineral mapping of the Semirom kaolin deposit in the Zagros fold-and-thrust belt, southwestern Iran. Spectral methods, including Band Ratio (BR), Relative Band Depth (RBD), Spectral Indices (SI), Principal Component Analysis (PCA), Directed Principal Component Analysis (DPCA), and Band Ratio Color Composite (BRCC), were employed to identify key industrial minerals such as kaolinite, calcite ($CaCO_3$), and hematite (Fe_2O_3). The results were used to generate reference datasets for training machine learning (ML) algorithms including Random Forest (RF) and Support Vector Machine (SVM) to delineate the spatial distribution of the target minerals. Remote sensing outputs were validated through field observations and X-ray diffraction (XRD) analyses, and classification performance was assessed using confusion matrices and the Kappa coefficient. In this context, the study pursues three main goals: (1) to identify and map key indicator minerals in the Semirom kaolin deposit using ASTER data, (2) to evaluate and compare the effectiveness of widely used spectral analysis techniques in delineating clay minerals and associated alteration patterns, and (3) to propose the most suitable remote sensing method for future applications in similar geological settings, thereby enhancing accuracy, reducing exploration costs, and supporting more efficient, targeted mineral exploration.

Geological Settings

The study area is located approximately 27 km southwest of Semirom city, within the High Zagros structural zone and specifically the Semirom subzone (Navaei & Mahdizadeh Tehrani, 1986). The Semirom clay deposit extends between 51°15′22″ to 51°34′56″ E and 31°09′40″ to 31°21′15″ N, as indicated on the 1:100,000-scale geological map of Kuh-e-Dena, near Posht-e Village. The deposit covers an area of about 30 km² and is accessible primarily via the Semirom-Yasuj road.

The stratigraphy of the region comprises Cretaceous formations (Darian, Kazhdumi, Sarvak, Ilam, and Gurpi), the Maastrichtian Tarbur Formation, the Pliocene Bakhtiari Formation, and Quaternary deposits (Alavi et al., 1996; Sedaghat & Gharib, 1999). The Dena Fault, characterized by thrusting and dextral strike-slip displacements, has exerted a major influence on the tectonic evolution of the area (Pattinson & Takin, 1971; Berberian, 1976; Comby et al., 1977).

Of particular geological importance is the Ilam Formation, which contains a clay-laterite horizon at its contact with the underlying Sarvak Formation. This horizon records a sedimentary hiatus accompanied by intense weathering, during which kaolinitic materials accumulated within voids, cavities, and karstic structures of the carbonate units. In some parts of the Zagros, this horizon locally developed into bauxitic layers under conditions of enhanced weathering and favorable physicochemical environments, reflecting advanced lateritization processes in warm and humid paleoclimates during the Late Cretaceous (Zamanian et al., 2016; Ahmadnejad et al., 2017; Ahmadnejad & Mongelli, 2023; Taghipour et al., 2024; Ahmadnejad & Rafat, 2025).

The tectonic framework of Iran, including its principal structural zones, is illustrated in Figure 1a to provide regional geological context. A more detailed overview of the Zagros orogenic belt is shown in Figure 1b, where the Semirom study area is marked with a black star. Furthermore, a simplified 1:100,000-scale geological map of the Kuh-e Dena quadrangle illustrates the local lithological framework (Figure 1c; Sedaghat & Gharib, 1999). where the kaolin horizon is marked with the code "CK".

The Semirom kaolin deposit lies at the unconformable contact between Upper Cretaceous carbonate units specifically the underlying Sarvak and overlying Ilam formations. Geochemical analyses of similar Upper Cretaceous deposits in the High Zagros structural zone indicate tropical weathering conditions (Ahmadnejad & Mongelli, 2023). The lower unit beneath the kaolin layer comprises interbedded limestones and calcareous shales, determined through microfossil analysis to belong to the Middle Cretaceous (Sarvak Formation). The upper unit consists of a dark grey fossiliferous limestone (~30–40 m thick), characterized by ammonite and rudist fossils, corresponding to the Middle Cretaceous Ilam Formation. The kaolin layer is hosted at the unconformity between these two formations (Salamab-Ellahi et al., 2019).

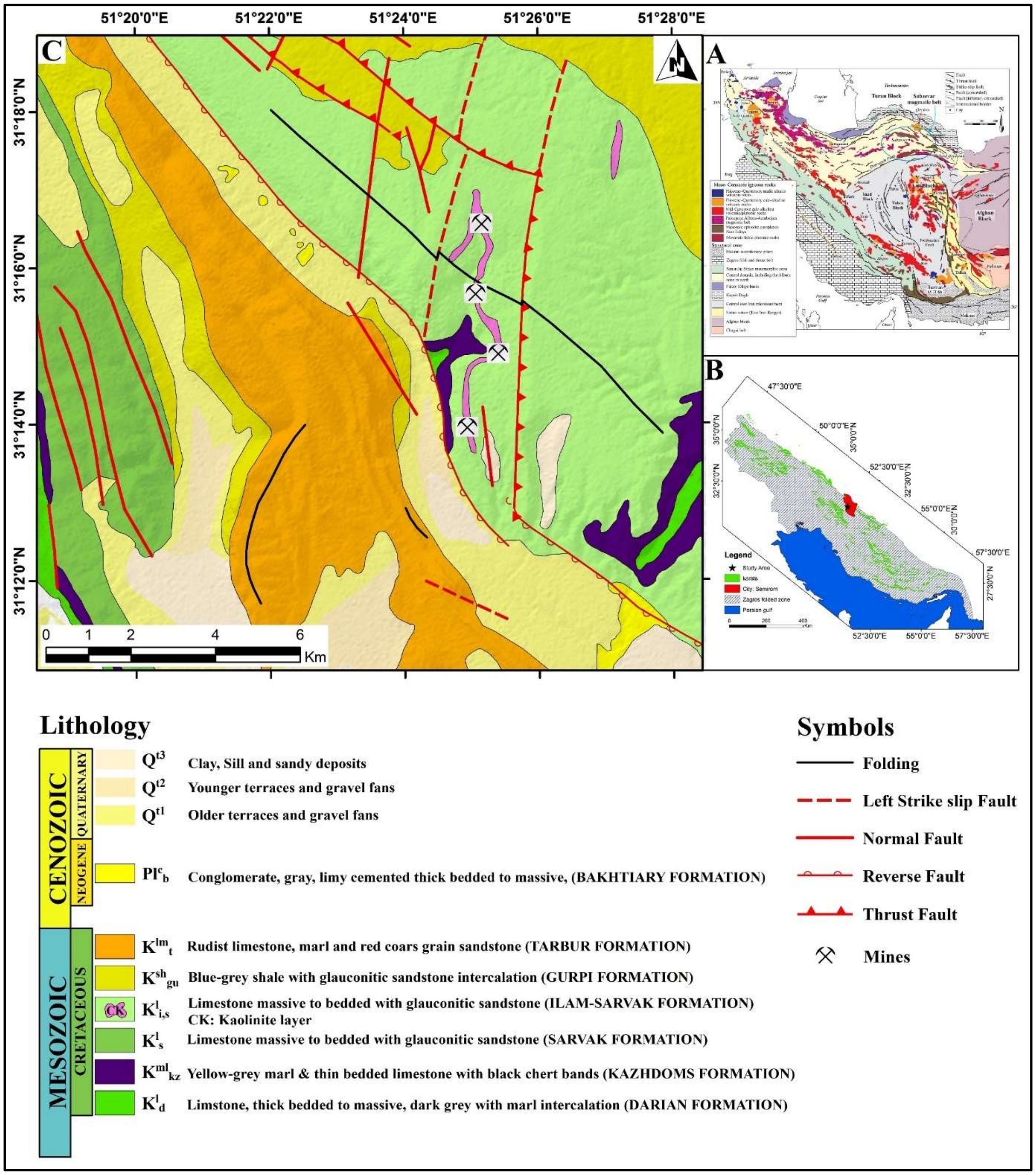

Figure 1. (a) Structural framework map of Iran illustrating the major tectonic zones (modified from Arjmandzadeh et al., 2022; after Arjmandzadeh et al., 2011; Berberian & King, 1981; Richards et al., 2012). (b) Detailed view of the Zagros structural zone, with the study area highlighted by a black star, showing its geographic location and surrounding topography. (c) Simplified 1:100,000-scale geological map of Kuh-e Dena illustrating the spatial distribution of stratigraphic units and the kaolinite-bearing horizon (CK) (modified from Sedaghat & Gharib, 1999)

The deposit comprises three major kaolinitic horizons: (a) the red clay horizon, distinctly colored due to high hematite ($Fe_2O_3 \approx 17.3\%$) content and lacking industrial value; (b) the main kaolin horizon, composed predominantly of kaolinite and anatase (TiO_2), with minor muscovite-illite and goethite ($FeO(OH)$) also detected in some samples. This unit includes Fe-rich bands with Fe_2O_3 concentrations ranging from 6% to 42%, significantly impacting ore quality; (c) the overlying marl–limestone interbedded horizon, characterized by diverse mineralogy including calcite ($CaCO_3$), kaolinite, illite ($(Al,Mg,Fe)_2(Si,Al)_4O_{10}[(OH)_2,(H_2O)]$), muscovite ($KAl_2(Si_3Al)O_{10}(OH,F)_2$), anatase, quartz, and goethite. Petrographic and XRD analyses further indicate the scattered presence of boehmite ($Al_2O_3 \cdot H_2O$) within the kaolin horizon. A schematic stratigraphic column illustrating the mineralized unit's position is presented in Figure 2 (Khaledi, 2022).

Historically, the ore was mined using underground techniques, but due to safety concerns, the current operation is conducted via open-pit methods, incorporating blasting and manual ore sorting on-site. The laterally continuous kaolin horizon, coupled with moderate variations in thickness and mineral composition, reflects a stable depositional setting during the formation of the deposit.

Materials & methods

Materials

The ASTER dataset used in this study was acquired on July 28, 2002, with a Level 1T (L1T) processing level. The granule ID is AST_L1T_00309262002072809_20150425085934_53682, provided by the United States Geological Survey (USGS) through the Earth Explorer platform (https://earthexplorer.usgs.gov/). The image was later radiometrically and geometrically corrected by USGS on April 25, 2015. ASTER, onboard the Terra satellite, collects multispectral data in three subsystems: the VNIR (3 bands), SWIR (6 bands), and TIR (5 bands). The dataset used in this study corresponds to Path 165 and Row 39, with zero cloud coverage, making it highly suitable for geological remote sensing applications.

Methodology

ASTER Level 1T data were utilized to map the distribution of clay minerals, carbonate minerals, and iron oxides in the study area (Figure 4). The SWIR bands of ASTER are affected by the well-documented "Crosstalk Effect," which results from energy spillover from Band 4 into Bands 5 and 9, leading to anomalously high radiance values (Jain et al., 2022). The dataset used in this study was pre-processed using the Crosstalk correction method (USGS, 2022). To remove atmospheric distortions and convert radiance to surface reflectance, the Internal Average Relative Reflectance (IARR) method was applied, which is particularly suitable for arid and semi-arid regions (Rani et al., 2017).

ASTER data, which cover a broad spectrum from the VNIR to SWIR and TIR ranges, enable the identification of distinct absorption features of minerals and rocks across a wide range of wavelengths. The spatial resolution of these bands (15 meters for VNIR, 30 meters for SWIR, and 90 meters for TIR) combined with a 60 km swath width per image, facilitates detailed lithological mapping and comprehensive geological analysis at multiple scales (Alarifi et al., 2022). Table 1 summarizes the specifications of the ASTER sensor, including the wavelength ranges of its various spectral bands.

Figure 3 illustrates the spectral behavior of key minerals, including kaolinite, hematite, and calcite, across the ASTER sensor bands, using reference spectra from the USGS spectral library.

Table 1. Sensor characteristics of ASTER instruments (Rajendran & Nasir, 2017).

Sensor's characteristics	**ASTER**		
	VNIR	**SWIR**	**TIR**
Spectral bands with range (µm)	**Band 01** 0.52–0.60	**Band 04** 1.6–1.7	**Band 10** 8.125–8.475
	Nadir looking		
	Band 02 0.63–0.69	**Band 05** 2.145–2.185	**Band 11** 8.475–8.825
	Nadir looking		
	Band 03N 0.76–0.86	**Band 06** 2.185–2.225	**Band 12** 8.925–9.275
	Nadir looking		
	Band 03B 0.76–0.86	**Band 07** 2.235–2.285	**Band 13** 10.25–10.95
	Backward looking	**Band 08** 2.295–2.365	**Band 14** 10.95–11.65
		Band 09 2.36–2.43	
Spatial Resolution (m)	15	30	90
Swath width (km)	60	60	60
Radiometric Resolution (bits)	8	8	12
Cross Track Pointing	± 318 km (± 24 deg)	± 116 km (± 8.55 deg)	± 116 km (± 8.55 deg)

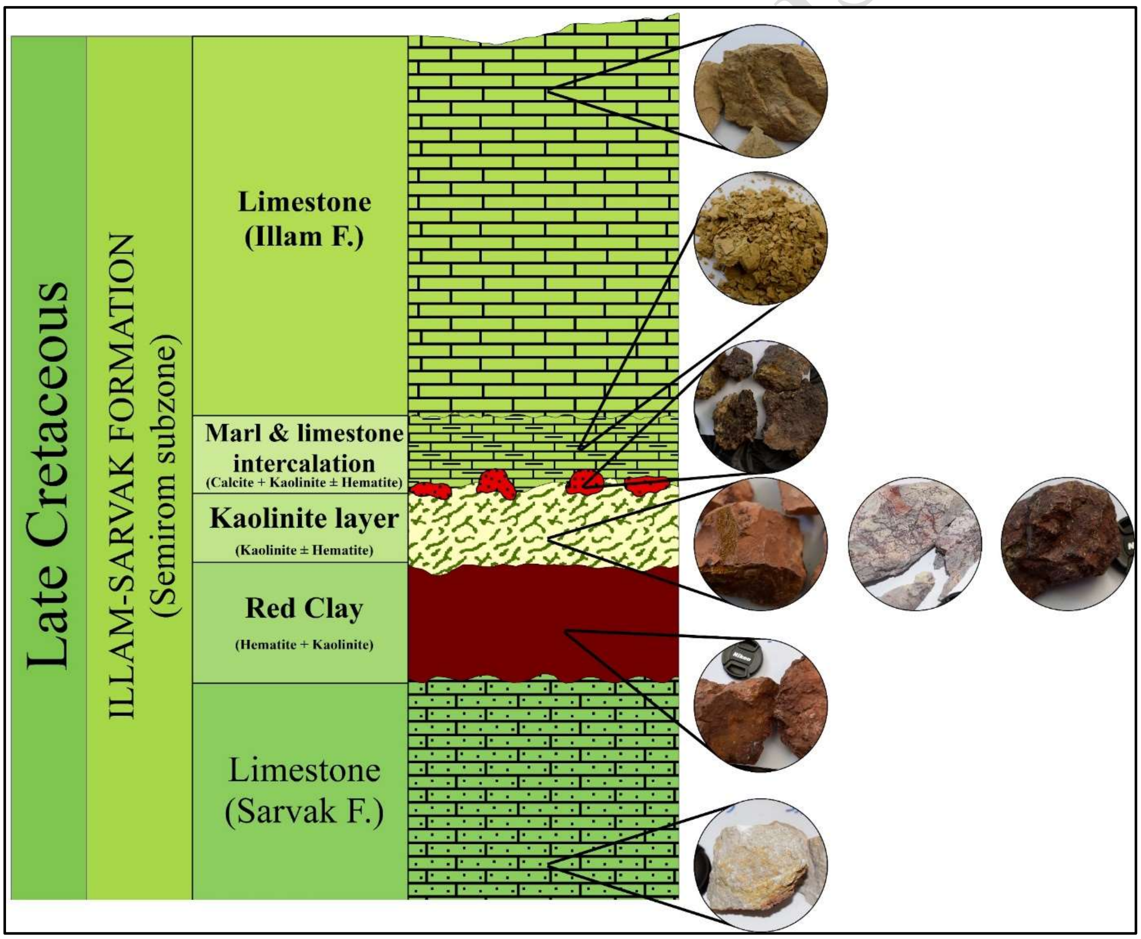

Figure 2. Schematic stratigraphic section of the Semirom kaolin deposit, illustrating the position of the kaolinitic layer at the unconformable boundary between the Sarvak and Ilam limestone formations, along with descriptions of the main horizons including the red clay horizon, the kaolin horizon, and the marl-limestone horizon (Khaledi, 2022)

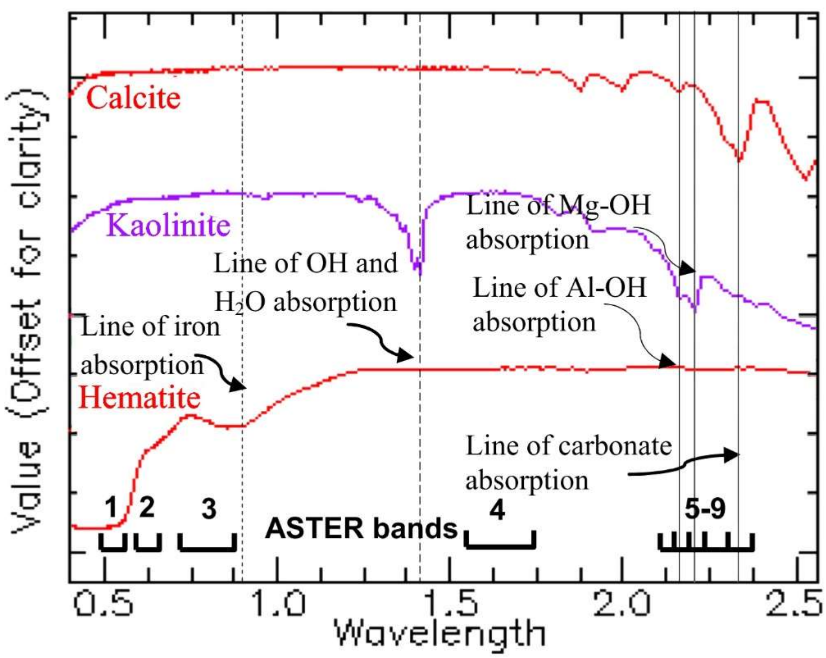

Figure 3. Laboratory spectra of minerals from hydrothermal alteration zones, including kaolinite, hematite, and calcite, obtained from the USGS Spectral Library (modified from Rajendran & Nasir, 2017)

A combination of spectral analysis techniques (including BR, RBD, Spectral Indices, PCA, DPCA, and Band BRCC) was applied to ASTER imagery to extract mineralogical information and discriminate among major industrial minerals, including kaolinite, calcite, and hematite.

The outputs of these spectral analyses were integrated to generate reference datasets, which were subsequently used as training inputs for supervised machine learning modeling in SAGA 9.9.1 software. Using these datasets, RF and SVM algorithms were applied to delineate the spatial distribution and extent of the target mineral phases.

Validation of the remote sensing–derived mineral maps was conducted through field studies across representative lithological units, and collected samples were analyzed using XRD at ZarAzma Laboratory (Iran) to determine their mineralogical composition and confirm the presence of clay minerals, iron oxides, and carbonate phases. Field and laboratory data were jointly used to ground-truth and refine interpretations derived from satellite imagery. The accuracy and reliability of mineral discrimination were quantitatively assessed using confusion matrices and the Kappa coefficient, providing a robust evaluation of the applied methodological framework (Figure 4).

Image processing algorithms

Band ratios (BR) and relative band depth (RBD) and Spectral Indices (SI)

The BR technique is based on selecting specific wavelengths where target minerals show diagnostic absorption or reflection characteristics, thereby allowing for targeted enhancement of mineral groups (Thurmond et al., 2006). Alternatively, the RBD approach involves calculating the ratio between spectral bands located on either side of an absorption feature (numerator) and the band representing the absorption minimum (denominator), which enables more accurate detection of minerals by incorporating absorption depth and normalizing illumination variability (Huo et al., 2014; Yan et al., 2014; Sengar et al., 2020).

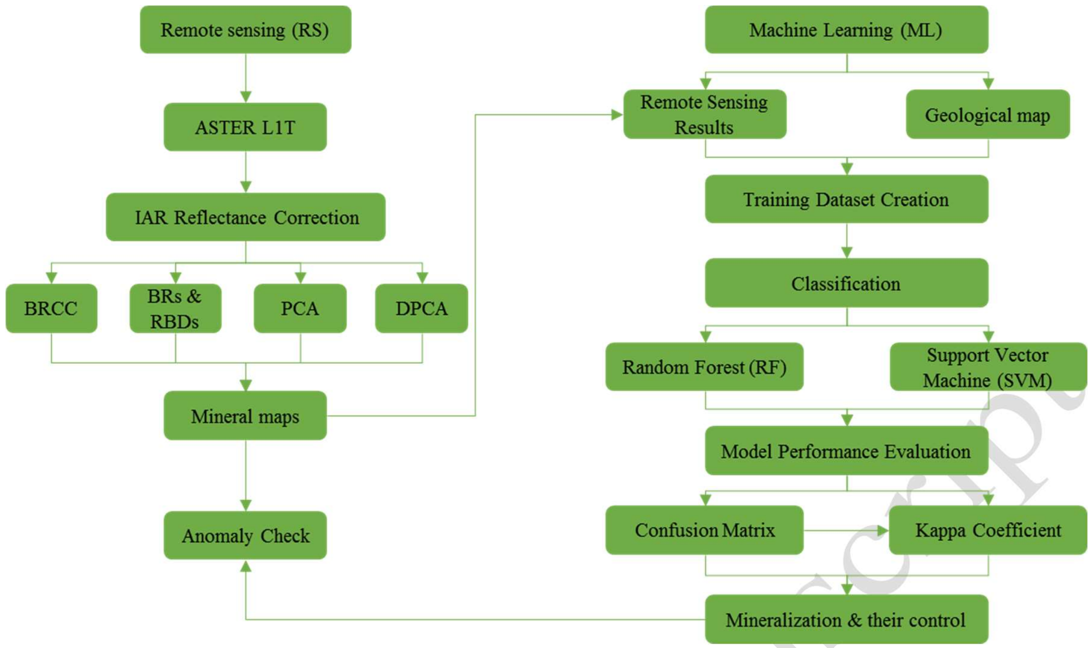

Figure 4. Schematic workflow of the present study. ASTER data were processed using BRCC, BR, PCA, and DPCA techniques within ENVI 5.3 and ArcGIS 10.8.2. The resulting outputs were validated through field observations and geochemical analyses, and subsequently used as training datasets for RF and SVM algorithms in SAGA 9.9.1. Model performance was assessed via confusion matrices and the Kappa coefficient, and final results were further verified through anomaly evaluation and field-based validation

Iron-rich lithologies typically exhibit absorption in the visible range, whereas minerals containing hydroxyl groups (e.g., clays) and carbonates show characteristic absorptions between 2.1 and 2.5 µm due to vibrational overtones and combinations. ASTER's bands 5 and 6 are sensitive to Al–OH absorptions (2.17–2.20 µm), while band 8 is suitable for detecting Mg-OH and CO_3^{2-} features around 2.33 µm (Jain, 2022).

Spectral indices in remote sensing are mathematical formulations involving specific spectral bands to highlight diagnostic features of certain minerals. These indices are designed based on known absorption or reflectance properties within particular wavelength ranges and have been applied for the detection of minerals such as calcite, quartz, and kaolinite. The Calcite Likelihood Index (CLI) , defined as (CLI) = (b6/b8)×(b9/b8), utilizes ASTER SWIR bands to emphasize spectral absorption features associated with calcite around 2.33–2.35 µm (Ninomiya, 2003). For kaolinite, the Kaolinite Index (KLI) is expressed as (KLI) = (b4/b5)×(b8/b6), targeting absorption features near 2.2–2.3 µm (Ninomiya et al., 2005). Quartz can be detected using thermal infrared indices such as (QI) = (b11+b12)/b10, which leverage the high emissivity of quartz between 8.5 and 9.5 µm. These indices are selected based on the spectral behavior of the target minerals and the capabilities of the imaging sensor, and they are commonly used to delineate alteration zones in mineral exploration (Rajendran & Nasir, 2017).

In this study, various BR, RBD, and spectral indices methods were applied to the atmospherically corrected ASTER data to map key industrial minerals, within the Semirom kaolin deposit (Table 2).

Principal Component Analysis (PCA) and Directed Principal Component Analysis (DPCA)

The PCA is a widely used statistical technique for reducing the dimensionality of multispectral data by transforming correlated spectral bands into a set of uncorrelated variables, referred to as principal components (PCs) (Sekandari et al., 2022).

Table 2. Description of BRs, RBDs and Spectral indices of the ASTER data used for mapping along with the characteristic spectral absorption features

No.	Mineral Group	Formula	Reference
VNIR & SWIR bands			
Band Ratio (BR)			
1.	Ferric iron oxides, Fe^{3+}	(b2/b1)	(Rowan & Mars, 2003)
2.	Fe + Al rich (Laterite)	(b4/b5)	(Hewson et al., 2005)
Relative Band Depth (RBD)			
3.	Alunite–kaolinite–pyrophyllite	(b4 + b6)/b5	(Rowan & Mars, 2003)
4.	Carbonate–chlorite–epidote	(b7 + b9)/b8	(Rowan & Mars, 2003)
Spectral Indices			
5.	Kaolinite	(KLI) = (b4/b5) × (b8/b6)	(Ninomiya et al., 2005)
6.	Calcite	(CLI) = (b6/b8) × (b9/b8)	(Ninomiya, 2003)

This transformation is based on the covariance or correlation matrix and helps to eliminate redundant information while retaining the primary features of the dataset (Reyment & Davis, 1988). PCA has been extensively utilized in lithological discrimination and hydrothermal alteration mapping and is particularly effective in minimizing the interference of surface cover such as vegetation (Kaufmann, 1988). However, conventional PCA may lead to suboptimal results when certain spectral bands that do not contribute significantly to the discrimination of target features are included in the analysis. To address this limitation, the DPCA technique was introduced by Crosta & M. Moore (1998). DPCA involves the selective use of spectral bands that exhibit the most diagnostic absorption or reflectance features associated with specific mineral phases. This selective approach enhances the sensitivity of the method to the desired geological targets and improves the interpretability of the outputs.

In this study, the DPCA method was applied to atmospherically corrected ASTER data for the identification of clay minerals, carbonates, and iron oxides. Relevant spectral bands were carefully selected based on their known diagnostic features for the target minerals. The resulting PCs were analyzed using eigenvector loadings to determine the components that most effectively differentiate the spectral response of the mineral groups. These optimized PCs were then used to support the mapping of lithological variations and surface mineral distribution in the study area.

Band Ratio Color Composite (BRCC)

The BRCC method is a widely adopted image enhancement technique in remote sensing for mineral exploration, particularly effective with ASTER imagery due to its rich spectral coverage in the VNIR and SWIR regions. This method involves computing spectral band ratios that emphasize specific mineralogical absorption features (such as Fe^{3+}, Al–OH, Mg–OH, and CO_3^{2-}) by reducing topographic and illumination effects through normalization of reflectance values (Rowan & Mars, 2003; Kanlinowski & Oliver, 2004). Selected band ratios (e.g., b2/b1 for iron oxides, (b4+b6)/b5 for Al–OH-bearing clays, b8/b5 for chlorite) are assigned to the red, green, and blue channels to create a false-color composite that visually enhances hydrothermal alteration zones (Madani & Emam, 2011; Tende et al., 2022). This approach enables rapid and intuitive discrimination of lithological and alteration units, often serving as a preliminary tool prior to more advanced classification techniques such as PCA or SAM (Salehi et al., 2019). The simplicity, computational efficiency, and interpretability of BRCC make it particularly useful in regional reconnaissance and early-stage mineral prospecting.

Implementation of Machine-Learning (ML) Algorithms

Machine learning, as a contemporary approach for geological and remote sensing data analysis, facilitates the extraction of complex patterns and nonlinear relationships among variables, making it a powerful tool for the identification and discrimination of mineralogical units. In this study, datasets derived from ASTER imagery processed using BR, BRCC, PCA, and DPCA techniques were compiled as training data. These datasets were then applied within supervised classification frameworks, specifically RF and SVM, to detect spectral patterns associated with clay minerals, carbonates, and iron oxides, and to generate mineralogical maps of the study area with enhanced accuracy.

Training Data and Machine Learning for Mineral Mapping

Considering the limited outcrops of the mineralized material within the study area and the relative homogeneity of the geological background, a total of 14 samples were collected from different units of the deposit. In addition to sampling, systematic field surveys were conducted, resulting in the identification and registration of 149 reference points. These points, with well-characterized mineralogical composition, were used as baseline geological data for machine learning modeling. The accuracy and reliability of these data were evaluated and confirmed through targeted field observations and petrographic analysis of thin sections.

Among the collected points, 31 were assigned to kaolin layers and identified as representative of kaolinite. 51 points corresponded to the Ilam–Sarvak limestone units and were registered as representative of calcite. In parts of the kaolin deposit floor, 15 points were collected from red clay layers, which, due to enrichment in hematite, caused the kaolin to acquire a reddish color, forming a distinct horizon. Additionally, to improve classification accuracy and prevent misattribution of other background units to the three main categories, 52 points were defined as background.

Figure 5 shows the sampling points and geological study stations. In this figure, sampling locations are indicated by green circles, limestone outcrops representing calcite accumulation are shown as yellow diamonds, kaolin layer outcrops are marked with blue stars, red clay layers containing kaolinite and hematite are indicated with red flags, and other points representing background are shown with black symbols.

Subsequently, the prepared training dataset was introduced to RF and SVM algorithms. In this study, a combination of ASTER spectral bands along with extracted features was used as input to the models, enabling accurate discrimination and mapping of the target mineralogical units.

Random Forest (RF)

The RF, developed by Breiman (2001), is an ensemble, tree-based learning algorithm and a robust non-parametric method widely used for addressing various data mining problems. Compared to single decision trees (DTs), RF is less sensitive to outliers and can accommodate diverse input data without overfitting. The algorithm constructs multiple DTs from randomly selected subsets of the training data. While DTs often suffer from overfitting due to their tendency to closely fit the training data (Gallatin & Albon, 2023), RF mitigates this issue by aggregating the outputs of individual trees. Specifically, RF employs averaging for regression tasks and majority voting for classification tasks (Dangeti, 2017), thereby improving predictive accuracy and reducing overfitting.

Support Vector Machine (SVM)

The SVMs, formally introduced by Cortes & Vapnik (1995), are advanced supervised machine learning algorithms extensively employed for both classification and regression tasks (Bahrami et al., 2022). The fundamental principle of SVM is to identify an optimal hyperplane that maximally separates the training data into predefined classes. This decision boundary is determined iteratively during the training process to minimize misclassification and enhance generalization. In high-dimensional feature spaces, the resulting hyperplane represents an (n−1)-dimensional subspace within an n-dimensional input space (Mountrakis et al., 2011).

A critical aspect of SVM is that only a subset of the training samples, termed support vectors, directly determines the position and orientation of the hyperplane. For datasets that are not linearly separable, SVM employs kernel functions to project input data into higher-dimensional spaces, thereby improving separability (Bahrami et al., 2024). Among the various kernel options, the radial basis function (RBF) kernel is widely adopted due to its effectiveness in capturing complex nonlinear relationships and enhancing model performance in nonlinear classification and regression scenarios (Dangeti, 2017).

Accuracy Assessment

A confusion matrix is commonly employed to evaluate the performance of classification algorithms. It summarizes the number of true positives (TP), true negatives (TN), false positives (FP), and false negatives (FN). In this context, TP refers to the number of pixels for which both ground-truth data and the machine learning algorithm assign the same positive label. FP represents instances where the true label is negative but the algorithm incorrectly predicts it as positive. FN denotes cases where the true label is positive but the prediction is negative. TN corresponds to samples correctly identified as negative by both ground-truth data and the algorithm.

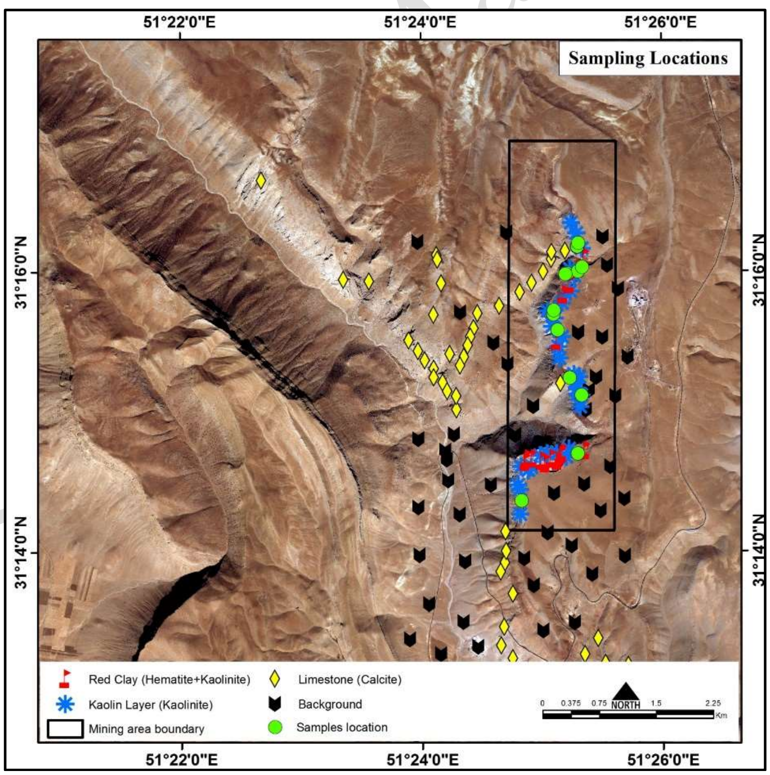

Figure 5. Sampling locations and reference points within the study area. Green circles and plus signs denote general sampling sites. Yellow diamonds indicate limestone outcrops with elevated calcite content. Blue stars represent kaolin-bearing layer exposures, while red flags mark red clay layers enriched in kaolinite and hematite. Black symbols correspond to background reference points. All locations were validated through field observations and laboratory analyses, providing reliable reference data for geological characterization and modeling of the Semirom kaolin deposit

$$Recall = \frac{TP}{TP+F}.. \tag{1}$$
$$Precision = \frac{FP}{TP+} \tag{2}$$
$$F1 - score = 2 \times \frac{Precision \times \text{Recall}}{Precision + \text{Recal}} = \frac{2 \times TP}{2 \times TP + FP + FN} \tag{3}$$
$$Accuracy = \frac{TP+T}{TP+FP+FN+TN} \tag{4}$$

Based on these definitions, three metrics were used to assess the performance of each class (Equations 1–3). In addition, overall accuracy (Equation 4) was calculated for each method by dividing the total number of correctly classified samples by the total number of samples (Story & Congalton, 1983).

Field checks and laboratory analysis

To verify and ground-truth the remote sensing interpretations, systematic field surveys were carried out across key alteration zones within the study area. Representative surface rock and soil samples were collected from selected sites exhibiting spectral signatures indicative of alteration. The collected samples were subjected to XRD analysis in order to identify and quantify the constituent mineral phases, with particular emphasis on carbonate minerals (e.g., calcite), clay minerals (e.g., kaolinite), and iron oxides (e.g., hematite, goethite). The mineralogical interpretation of the XRD patterns was conducted using the American Mineralogist Crystal Structure Database (AMCSD) as a reference standard. These results provided crucial validation for the satellite-based mineral mapping and aided in refining the remote sensing-derived mineral distribution models.

Results

In this study, a comprehensive and integrated suite of advanced processing techniques was applied to ASTER imagery to identify, discriminate, and assess the spatial distribution of minerals within the Semirom kaolin deposit and adjacent areas. The methodologies included BR, RBD, spectral indices, PCA, DPCA, BRCC, and supervised machine learning algorithms (RF and SVM). The following sections present the results obtained from the implementation of these methods and evaluate their performance in distinguishing the mineral assemblages of the study area.

BR, RBD, and Spectral Indices methods

The initial outcomes derived from the implemented spectral processing techniques are presented as grayscale images, where pixel intensity ranges from white (indicating minimal presence of target minerals) to black (indicating higher probability of occurrence). To enhance visual interpretability and facilitate more accurate assessment, the grayscale representations were further refined. In the enhanced visualization, pixels with the lowest likelihood of hosting the target mineral appear in white, while those with the highest probability are rendered in dark brown. This adjustment significantly improves the clarity of spatial mineral distributions.

Additionally, for each processed output, a zoomed-in inset of the active mining zone within the Semirom kaolin deposit is provided alongside the full-scene imagery. These inset figures allow for a detailed inspection of the extraction front. The boundaries of the current open-pit excavation are clearly delineated using bold blue lines, providing a precise visual reference for comparing remote sensing results with ground-truth mining activity.

The results of the BR, RBD, and spectral Indices methods, derived from the formulas listed in Table 2, are collectively illustrated in Figure 6 due to their methodological similarities and comparable outputs. Figure 6a displays the enhanced detection of ferric iron-bearing minerals such as hematite, mapped using the BR technique (b2/b1), which corresponds to widespread hematite-rich layers across the study area. Similarly, Figure 6b highlights the delineation of lateritic surfaces using the BR method (b4/b5), reflecting the lateral extent of laterite horizons identified in the region.

For clay minerals, particularly kaolinite Figure 6c and Figure 6d present the output of the RBD ((b4 + b6)/b5) and spectral index methods ((b4/b5)×(b8/b6)), respectively. These techniques reveal the surface distribution of kaolinite-bearing units with considerable precision. Furthermore, to identify carbonate minerals such as calcite (crucial for distinguishing between pure limestone units and other carbonate-bearing formations) the RBD method ((b7 + b9)/b8) (Figure 6e) and relevant spectral indices ((b6/b8)×(b9/b8)) (Figure 6f) were applied. Each figure corresponds to distinct spectral parameters tailored to the mineralogical features of interest, ensuring optimal contrast and feature enhancement.

PCA and DPCA analysis

To enhance the mineralogical interpretation of ASTER satellite data, two statistical techniques (PCA and DPCA) were independently applied to identify and delineate the spatial distribution of key minerals within the study area. These methods leverage spectral variance across VNIR and SWIR bands to improve detection sensitivity for mineralogical anomalies. The primary focus was on mapping the distribution of hematite, kaolinite, and calcite, with outputs visualized as mineral probability maps.

For PCA, nine ASTER bands covering VNIR and SWIR ranges were utilized. Based on eigenvector loadings, optimal components for each mineral were selected according to their characteristic absorption and reflectance features as identified in established spectral libraries (Table 3). Hematite, which exhibits strong absorption in Band 3 (0.76–0.86 μm) and prominent reflectance in Band 1 (0.52–0.60 μm) (Abrams et al., 1988; Hunt, 1977; Rajendran, 2009), showed its highest spectral response in PC4. Kaolinite, with absorption around Band 5 (2.145–2.185 μm) and reflectance in Band 8 (2.295–2.365 μm) (Mars & Rowan, 2011; Rajendran et al., 2011; Rajendran & Nasir, 2017), was best represented by PC3 and PC8. Calcite, characterized by absorption in Band 9 (2.36–2.43 μm) and reflectance across Bands 7 and 8 (Gaffey, 1986; van der Meer, 1994), exhibited the most significant contrast in PC5, with a negative loading. The mineral distribution maps derived from PCA are illustrated in Figures Figure 7a (hematite), Figure 7c (kaolinite), and Figure 7e (calcite).

DPCA was then applied to enhance discrimination by focusing on diagnostic absorption features through selective band combinations. For hematite/goethite, Bands 1 and 3 were used, and the mineral response peaked in PC2 (

Table ***4***; Figure 7b). Kaolinite was analyzed using Bands 5, 7, and 8, with the strongest signal occurring in the third principal component, specifically –PC3 (Table 5; Figure 7d). For calcite, Bands 8 and 9 were employed, revealing the most pronounced spectral response in PC2 (Table 6; Figure 7f).

BRCC

To enhance the visual interpretation of surface mineralogical features and vegetation cover within the Semirom kaolin deposit, the BRCC method was applied to ASTER imagery using selected VNIR and SWIR bands. This method involves generating band ratio images that emphasize specific spectral features by normalizing reflectance values, thereby minimizing topographic and illumination effects. Three diagnostic band ratios were calculated: Band3 to Band2 (B3/B2) to highlight vegetation cover, Band4 to Band1 (B4/B1) to enhance iron oxide signatures, and Band 4 to Band 6 (B4/B6) to target clay-rich zones.

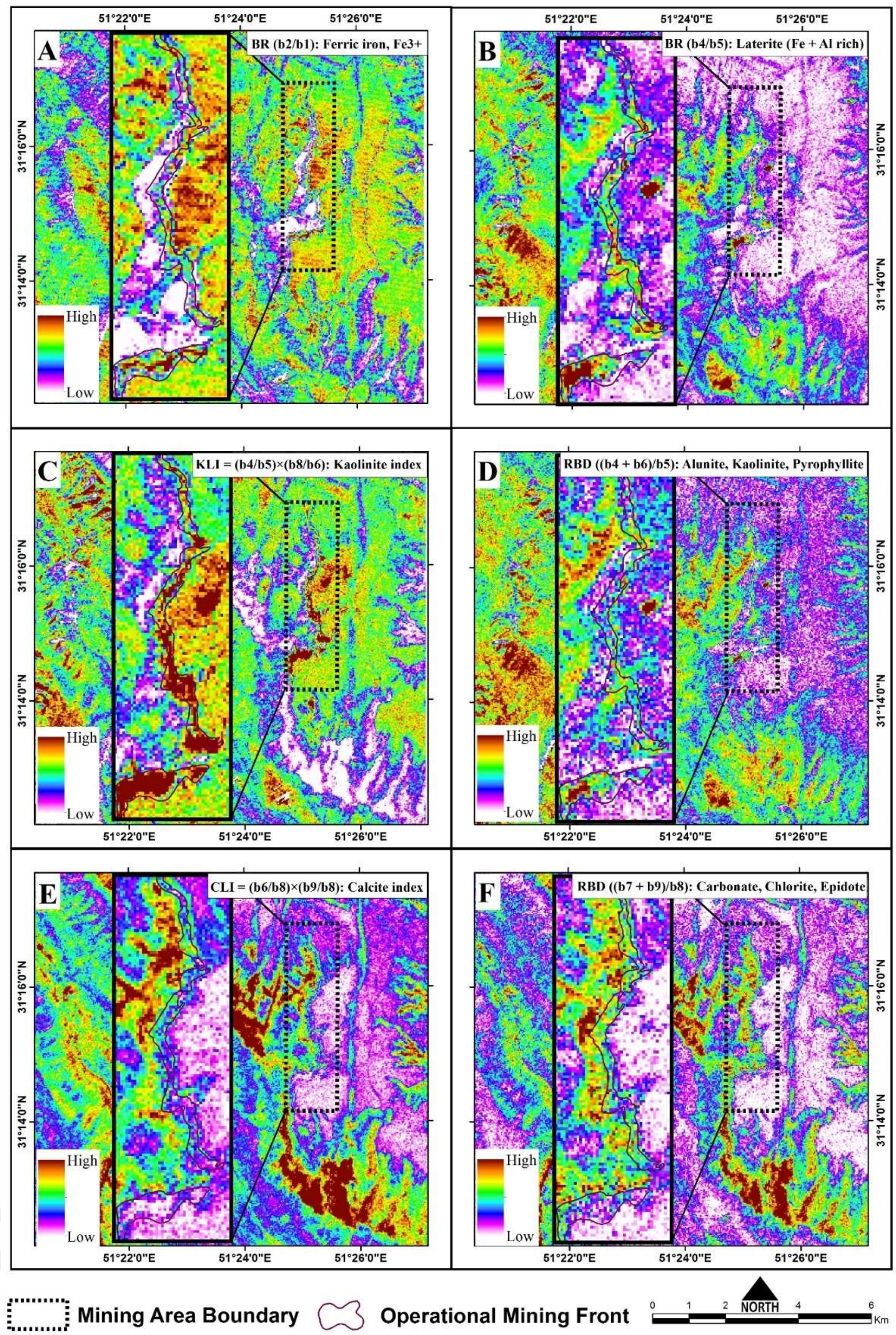

Figure 6. Enhanced mineralogical mapping results over the Semirom kaolin deposit and surrounding areas using ASTER satellite imagery and band-based processing techniques. (a) Detection of ferric iron-bearing minerals, including hematite, using BR; (b) delineation of lateritic surfaces via BR; (c) spatial distribution of kaolinite mapped through RBD; (d) identification of kaolinite using mineral-specific spectral indices; (e) mapping of calcite-rich carbonate rocks using RBD; and (f) delineation of carbonate units based on spectral indices analysis. For each map, the active mining zone is zoomed in and displayed in an inset panel to highlight the extraction area. The extent of the current open-pit working face is clearly outlined in bold blue lines. Color gradients in the maps represent the relative likelihood of target mineral presence, with white indicating the lowest and dark brown the highest probability

Table 3. PCA eigenvector loadings for selected components used in mapping hematite, kaolinite, and calcite from ASTER VNIR and SWIR bands

	Band 1	Band 2	Band 3	Band 4	Band 5	Band 6	Band 7	Band 8	Band 9
PC1	0.339999	0.357493	0.318763	0.348314	0.328739	0.346183	0.326747	0.316219	0.314638
PC2	-0.44446	-0.44983	-0.46023	0.025003	0.247898	0.228548	0.306231	0.311377	0.288538
PC3	0.070833	0.213259	0.016041	-0.59931	-0.1759	-0.34688	0.19453	0.63055	0.058063
PC4	0.68567	0.00828	-0.63678	-0.21149	0.107543	0.071461	0.052387	-0.22124	0.10587
PC5	0.228019	-0.18714	-0.17033	0.385623	-0.06919	0.015458	0.032361	0.454325	-0.72304
PC6	-0.39173	0.703467	-0.33896	-0.07191	0.155609	0.172504	0.181331	-0.13865	-0.35431
PC7	0.072296	-0.2932	0.361943	-0.50011	0.483221	0.227463	0.242843	-0.17237	-0.39213
PC8	0.015413	-0.06563	0.027563	0.235237	-0.05057	-0.5569	0.731878	-0.30084	-0.02253
PC9	-0.02806	0.064387	-0.07183	0.121769	0.723124	-0.55733	-0.36101	0.103237	0.023949

Table 4. DPCA eigenvector loadings for hematite detection using ASTER Bands 1 and 3 (PC2 selected)

	Band 1	Band 3
PC1	0.727663	0.685935
PC2	-0.68594	0.727663

Table 5. DPCA eigenvector loadings for kaolinite using ASTER Bands 5, 7, and 8 (–PC3 selected)

	Band 5	Band 7	Band 8
PC1	-0.57512	-0.58316	-0.57372
PC2	-0.66816	-0.06979	0.740735
PC3	0.472007	-0.80935	0.349514

Table 6. DPCA eigenvector loadings for calcite using ASTER Bands 8 and 9 (PC2 selected)

	Band 8	Band 9
PC1	0.719663	0.694323
PC2	-0.69432	0.719663

These ratios were respectively assigned to the red, green, and blue channels of the color composite (Xu et al., 2004). Figure 8a-c illustrates the individual grayscale ratio images corresponding to vegetation, iron oxides, and clay minerals. In these images, brighter areas (closer to white) indicate higher probability of the presence of the target feature, whereas darker areas represent lower values. For spatial reference, the boundary of the active mining area has been delineated in yellow across all grayscale images.

The final false-color composite (Figure 8d) visually integrates these three spectral indicators. Areas with dominant vegetation appear in red, zones enriched in iron oxides in green, and clay-bearing surfaces in blue. Regions where all three characteristics coincide (typically representing agricultural lands) are shown in shades of white to pink, reflecting the combined spectral contributions of vegetation, clay minerals, and iron oxides. To support field validation, an inset displaying a zoomed view of the active mining front is included, clearly marked with bold outlines to correlate remote sensing results with current extraction activities.

ML Algorithms

RF

RF classification was performed on the Semirom kaolin deposit, and the resulting map was visualized in GIS. In the map, pixels representing calcite are shown in green, kaolinite in red, hematite in blue, and background pixels in black. The overall accuracy of the classification was 69.13%, with a Kappa coefficient of 0.546. Class-specific accuracies were as follows: calcite, producer accuracy 68.63% and user accuracy 100%; hematite, producer accuracy 46.67% and user accuracy 100%; kaolinite, producer accuracy 29.03% and user accuracy 56.25%; and background, producer accuracy 100% and user accuracy 57.14%. Commission and omission errors for each class were also recorded in the confusion matrix (Table 7). The classification map (Figure 9), together with these quantitative metrics, provides a comprehensive representation of the spatial distribution of the minerals within the study area.

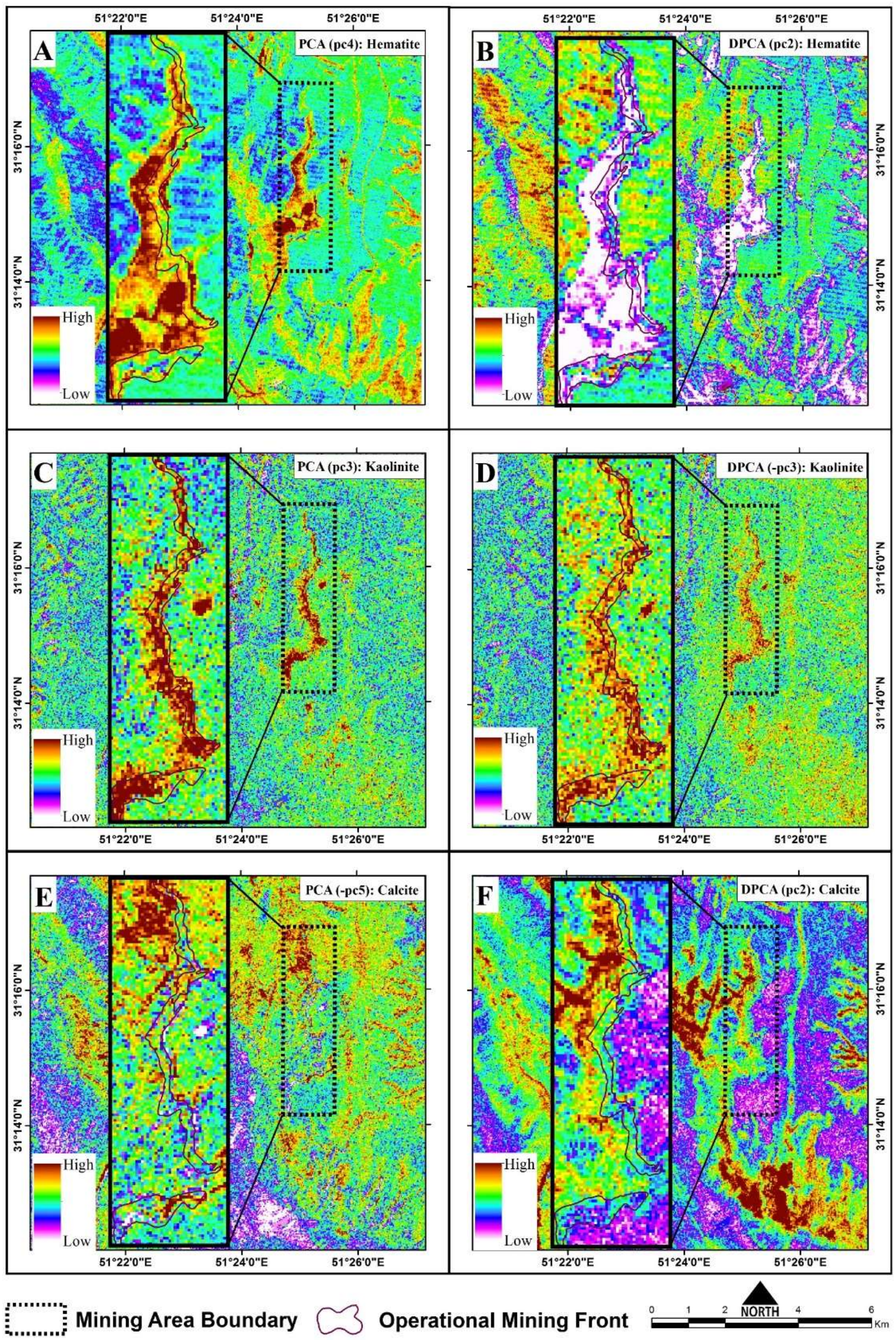

Figure 7. Mineral distribution maps generated from PCA and DPCA methods applied to ASTER data: (a) Hematite (PCA PC4), (b) Hematite (DPCA PC2), (c) Kaolinite (PCA PC8), (d) Kaolinite (DPCA PC3), (e) Calcite (PCA PC5), and (f) Calcite (DPCA PC2). Insets show zoomed-in views of the active mining zone, delineated with blue outlines for clarity

Table 7. Confusion matrix and accuracy assessment of the RF classification applied to the Semirom kaolin deposit. The table includes both pixel counts and percentages for each class, providing quantitative evaluation of classification performance. Overall accuracy and Kappa coefficient are reported to assess reliability

Class	Background	Calcite	Hematite	Kaolinite	Total
Background	52 (100%)	16 (31.37%)	1 (6.67%)	22 (70.97%)	91 (61.07%)
Calcite	0 (0%)	35 (68.63%)	0 (0%)	0 (0%)	35 (23.49%)
Hematite	0 (0%)	0 (0%)	7 (46.67%)	0 (0%)	7 (4.70%)
Kaolinite	0 (0%)	0 (0%)	7 (46.67%)	9 (29.03%)	16 (10.74%)
Total	52	51	15	31	149

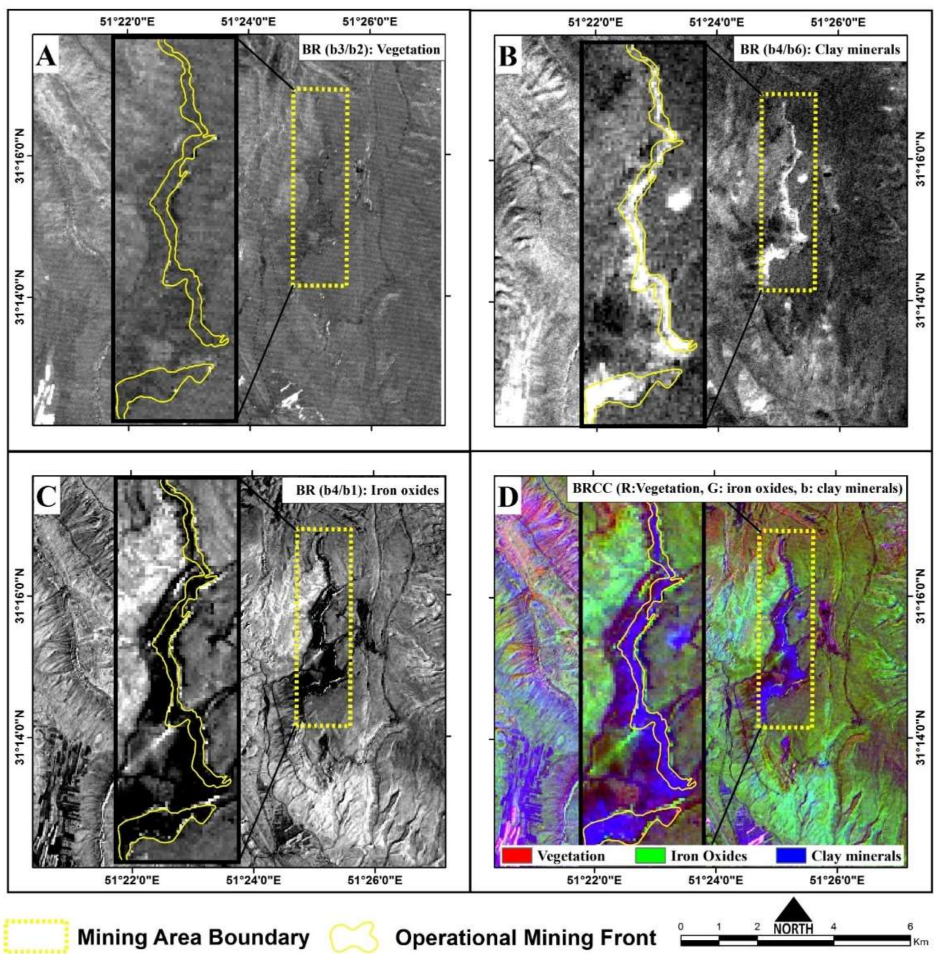

Figure 8. Grayscale band ratio images for (A) vegetation (B3/B2), (B) iron oxides (B4/B1), and (C) clay minerals (B4/B6), along with (D) the resulting false-color BRCC image. Brighter tones indicate higher presence of the target feature. The yellow outline marks the active mining boundary

SVM

SVM classification was applied to the Semirom kaolin deposit, and the resulting map was visualized in GIS. In the map, pixels representing calcite are shown in green, kaolinite in red, hematite in blue, and background areas in black. The overall accuracy of the classification was 77.18%, with a Kappa coefficient of 0.671.

Table 8. Confusion matrix and accuracy assessment of the Support Vector Machine classification applied to the Semirom kaolin deposit. Both pixel counts and percentages are reported for each class, and overall accuracy along with Kappa coefficient are included to provide a robust evaluation of classification reliability

Class	Background	Calcite	Kaolinite	Hematite	Total
Background	52 (100%)	16 (31.37%)	13 (41.94%)	0 (0%)	81 (54.36%)
Calcite	0 (0%)	35 (68.63%)	0 (0%)	0 (0%)	35 (23.49%)
Kaolinite	0 (0%)	0 (0%)	17 (54.84%)	4 (26.67%)	21 (14.09%)
Hematite	0 (0%)	0 (0%)	1 (3.23%)	11 (73.33%)	12 (8.05%)
Total	52	51	31	15	149

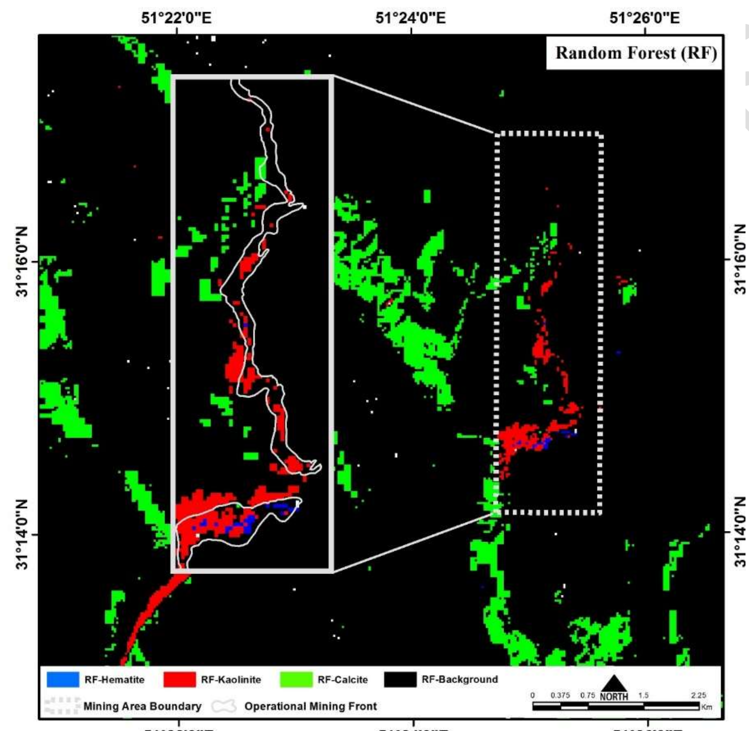

Figure 9. RF classification map of the Semirom kaolin deposit. Pixels representing calcite are shown in green, kaolinite in red, hematite in blue, and background areas in black. The map illustrates the spatial distribution of major mineral phases as identified by the RF algorithm, providing a visual representation of the mineralogical heterogeneity across the study area

Class-specific accuracies were as follows: background, producer accuracy 100% and user accuracy 64.20%; calcite, producer accuracy 68.63% and user accuracy 100%; kaolinite, producer accuracy 54.84% and user accuracy 80.95%; and hematite, producer accuracy 73.33% and user accuracy 91.67%. Commission and omission errors for each class were also recorded in the confusion matrix (Table 8). The resulting classification map (Figure 10), together with these quantitative metrics, provides a detailed representation of the spatial distribution of the major mineral phases within the study area.

Field Observations and XRD Mineralogy

Geological Field Observations

Two systematic field campaigns were conducted in the Semirom kaolin deposit to verify and complement remote sensing results. During these surveys, several lithological units were observed, including the lower limestone (Sarvak Formation), the red clay layer (unit d), the kaolin layer (unit c), alternating marl and limestone with pisolitic bands (units a and b), and the upper limestone (Ilam Formation) (Khaledi, 2022). These units are exposed either across the study area or in localized zones and are illustrated in panoramic views in Figure 11a and Figure 11b. Additionally, pisolitic iron-rich bands were observed within the kaolin-bearing strata (Figure 11c).

Sample Collection and Location Mapping

Rock samples were collected from multiple locations across different lithological units. The spatial distribution of the sampling points was plotted on a high-resolution Bing Map satellite image to ensure precise documentation (Figure 12). A zoomed-in view of the active mining face is also included to improve visibility of the sampling locations.

Petrographic Analysis

Petrographic investigations were performed on selected samples using thin and polished thin sections. Sample K-3-1, collected from the kaolin layer, exhibited a cryptocrystalline to clastic texture with a fine-grained kaolinite matrix. Scattered opaque minerals were observed within the groundmass (Figure 13a and Figure 13b). In sample G2-3-8, obtained from the iron-bearing pisolitic bands within the kaolin unit, iron oxides and hydroxides were identified under reflected light microscopy (Figure 13c and Figure 13d).

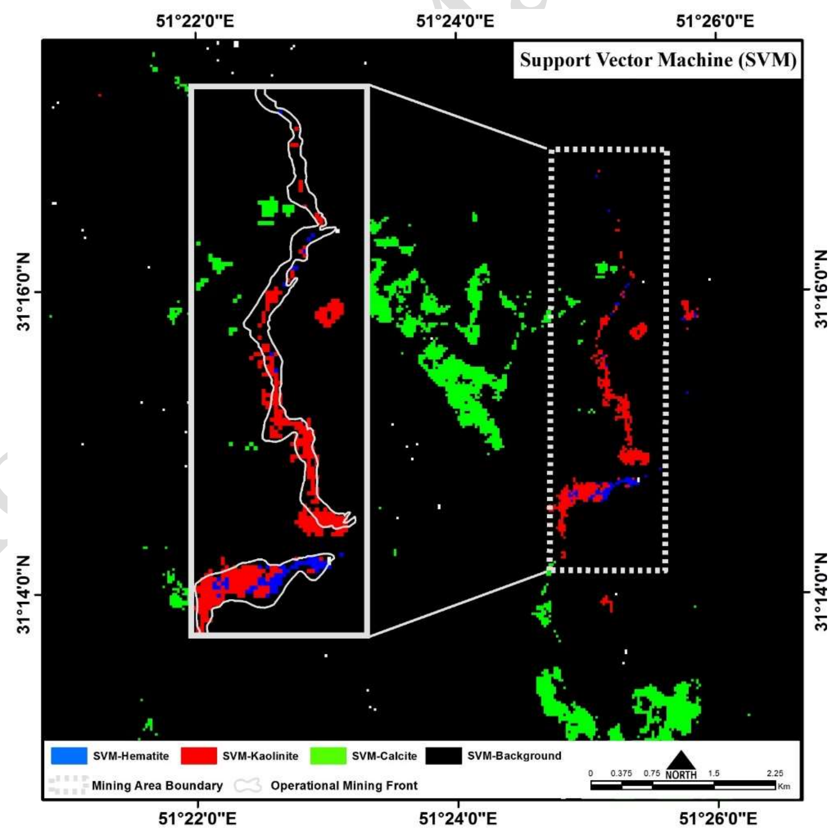

Figure 10. SVM classification map of the Semirom kaolin deposit. Pixels representing calcite are shown in green, kaolinite in red, hematite in blue, and background areas in black. The map depicts the spatial distribution of major mineral phases as identified by the SVM algorithm, providing a visual representation of mineralogical heterogeneity across the study area

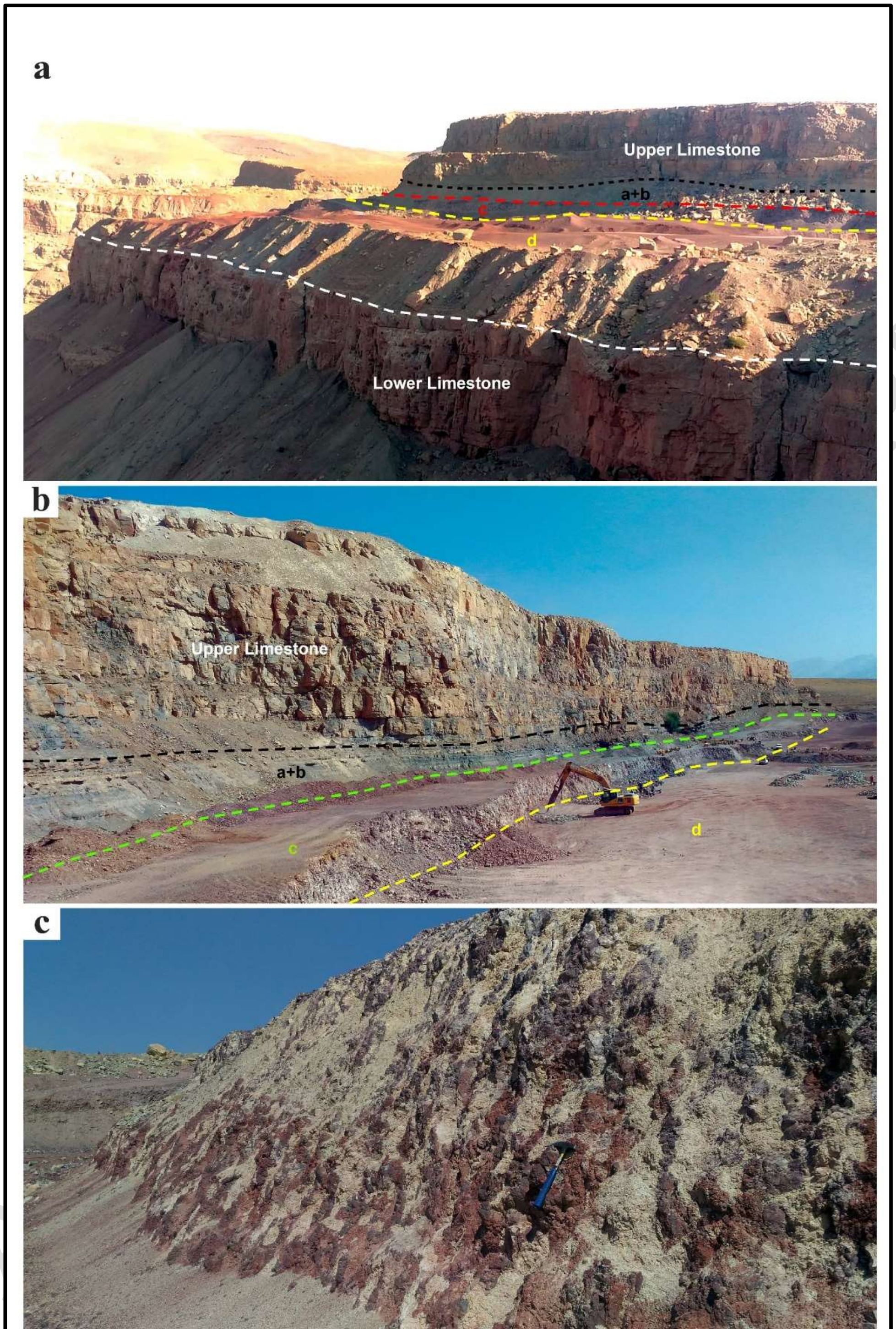

Figure 11. Field photographs from the Semirom kaolin deposit illustrating the main lithological units and their spatial relationships. (a) General view of the deposit looking north, showing the overall stratigraphy including the lower limestone (Sarvak Formation), red clay (unit d), kaolin layer (unit c), pisolitic marl-limestone alternations (units a and b), and upper limestone (Ilam Formation); (b) Eastward view highlighting the red clay, kaolin layer, pisolitic units, and upper limestone, excluding the Sarvak limestone due to limited exposure; (c) North to northeast view showing iron-rich pisolitic concentrations occurring as irregular, vein-like features extending upward from the base of the kaolin horizon

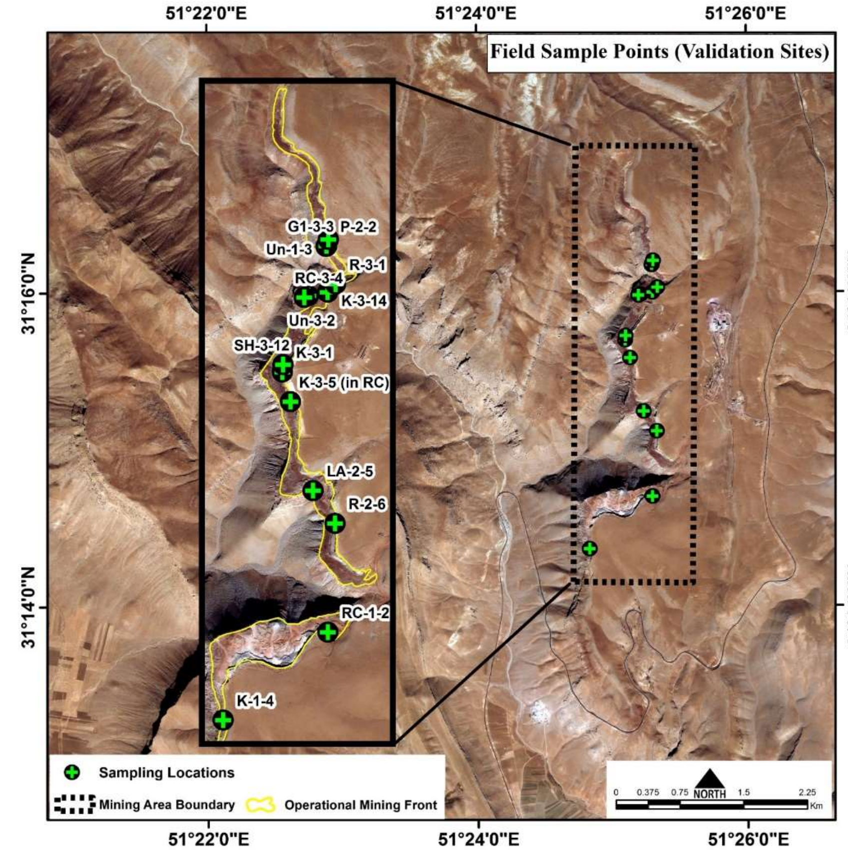

Figure 12. Sampling locations across the Semirom kaolin deposit, plotted on a high-resolution Bing Map image. A zoomed-in inset highlights the active mining front to provide a clearer view of individual sample points and their spatial distribution

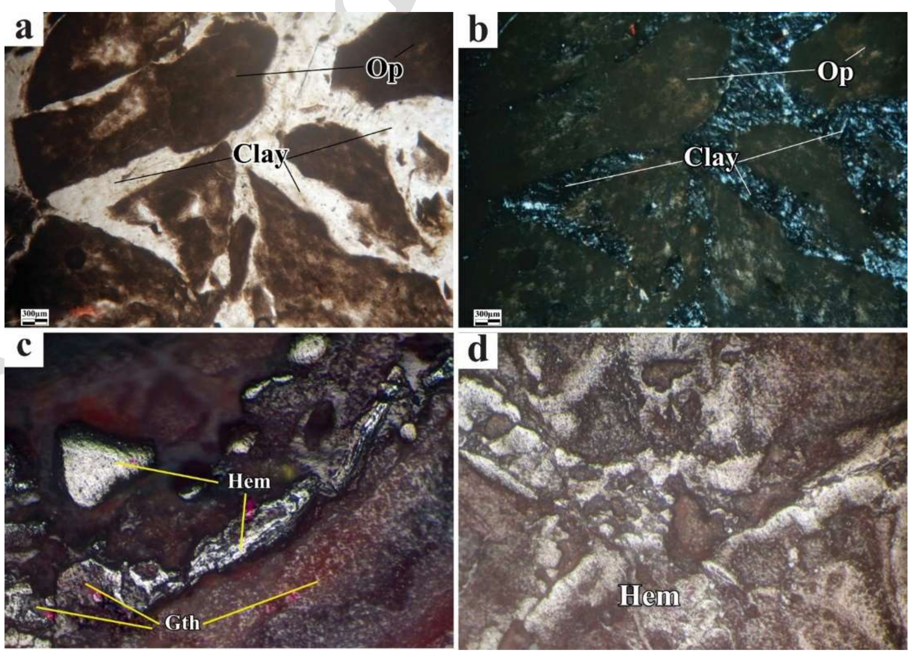

Figure 13. Thin section images of representative samples from the Semirom kaolin deposit. (a) PPL and (b) XPL views of sample K-3-1 showing fine-grained kaolinite (Clay) with dispersed opaques (Op). (c, d) Reflected light (100×) images of sample G2-3-8 illustrating hematite (Hem) and goethite (Gth) within the Fe-rich pisolitic zone

X-ray Diffraction (XRD) Analysis

The XRD patterns of selected samples are presented in Figure 14. The results confirm the presence of kaolinite, calcite, hematite, goethite, illite, anatase, and rutile in various lithological horizons across the deposit (Table 9).

Table 9. XRD results showing major, minor, and trace mineral phases in selected samples from the Semirom kaolin deposit

Name	Major Phase(s)	Minor Phase(s)	Trace Phase(s)
SH-3-12	Calcite	Quartz-Illite	-
UN-3-2	Amesite-Hematite-Kaolinite	Goethite	Anatase
UN-1-3	Hematite-Kaolinite	Goethite-Calcite	Anatase
P-2-2	Calcite-Kaolinite-Chlorite-Illite	Anatase	Goethite-Hematite
R-2-6	Calcite-Kaolinite-Illite	Anatase-Quartz-Goethite	-
R-3-1	Calcite-Illite-Kaolinite	Goethite-Quartz	Anatase
G1-3-3	Hematite-Kaolinite	-	-
K-3-14	Kaolinite	Anatase	Rutile
K-3-1	Kaolinite	Goethite	Rutile
K-1-4	Kaolinite	Anatase-Muscovite-Illite	-
K-3-5 (in RC)	Kaolinite	Hematite-Anatase-Muscovite-Illite-Goethite	Rutile
RC-3-4	Hematite-Kaolinite	Anatase-Bohmite-Goethite	-
RC-1-2	Kaolinite-Illite-Calcite	Hematite-Goethite-Anatase	Rutile
LA-2-5	Calcite	-	-

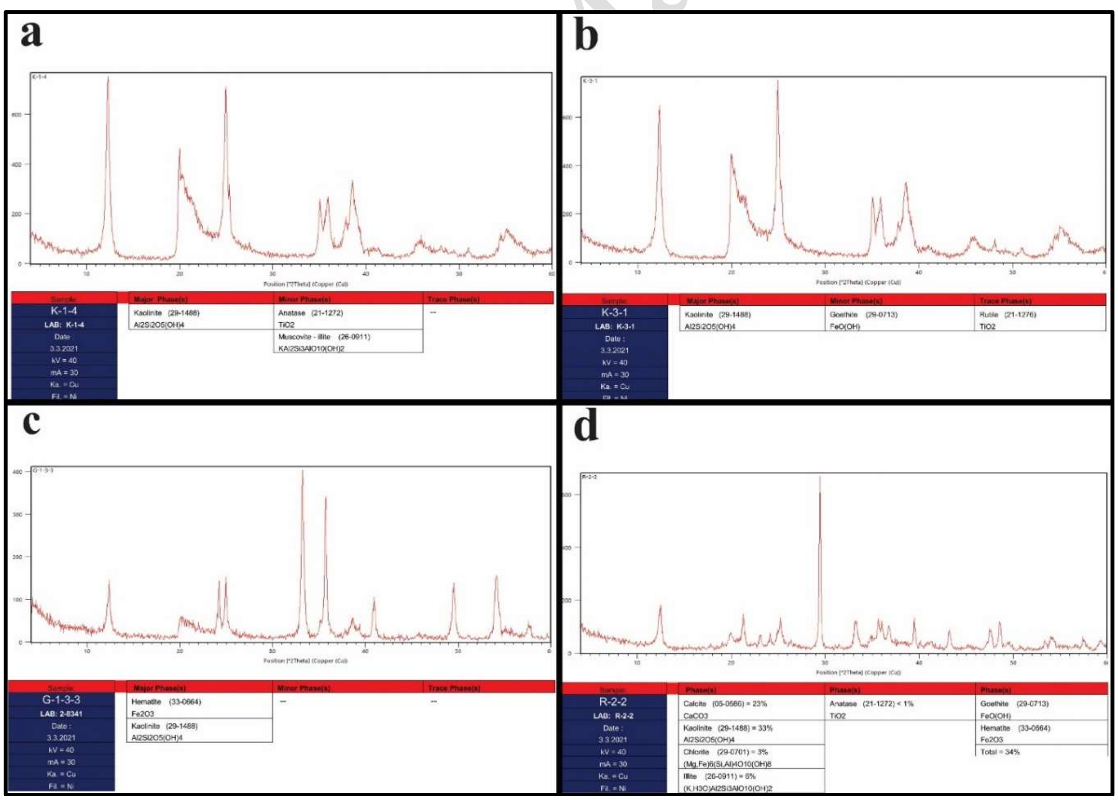

Figure 14. XRD patterns of selected samples from the Semirom kaolin deposit. (a, b) Samples K-1-4 and K-3-1 from the kaolin ore layer, with kaolinite as the dominant phase. (c) Sample G-1-3-3 from Fe-rich pisolitic veins within the ore layer, showing hematite as the major and kaolinite as the minor phase. (d) Sample R-2-6 from the overlying marl layer, containing calcite, kaolinite, chlorite, and illite as major phases

Discussion

The results obtained from various ASTER image processing techniques demonstrate that each method, depending on its spectral resolution and inherent analytical capacity, provides different levels of success in detecting the target minerals (kaolinite, hematite, and calcite). These variations highlight the complex interplay between geological conditions, spectral properties of the minerals, and the degree of surface exposure.

Analysis of BR, RBD and Spectral Indices

The BR technique, although it has demonstrated acceptable results in identifying iron-bearing minerals such as hematite in similar studies, failed to adequately reflect the spatial distribution of this mineral within the deposit (Figure 6a). This deficiency can primarily be attributed to spectral interference between hematite and clay minerals, particularly kaolinite. Clay minerals like kaolinite, with strong absorption features in the SWIR region, can effectively obscure the spectral signature of hematite (especially when hematite occurs in a dispersed and matrix-bound form within clay-rich setting).

Regarding laterites, despite the presence of ferruginous layers in the study area, the band ratio formula was unable to provide an accurate depiction of their distribution (Figure 6b). This limitation likely stems from erosional processes and geometric surface alterations of the mineralized material. The degradation and displacement of upper layers due to mining activities have exposed a red clay horizon (composed of a mixture of hematite and kaolinite) whose dominant clay signal in the imagery has masked the hematite signature.

In contrast, the KLI successfully delineated the full extent of kaolinite across the deposit (Figure 6c), a result that was corroborated by field observations and XRD analyses. Conversely, the RBD method showed limited success in identifying kaolinite (Figure 6d). This discrepancy can be explained by the mathematical nature of each approach: while KLI utilizes a multi-band ratio that combines absorption and reflectance features, RBD is highly sensitive to absorption depth and may underperform due to noise or surface cover.

For calcite, both the CLI and RBD methods identified similar zones, which were consistent with field observations (Figure 6e and Figure 6f). However, the mapped distribution was less extensive than expected. This underrepresentation is likely due to surface coverage by secondary or erosional deposits, which can suppress the satellite reflectance signal of underlying limestone bedrock.

Performance of PCA and DPCA Methods

In the case of hematite, the PCA yielded somewhat scattered results. Although parts of the PCA output correlate well with ground truth, other parts diverge significantly (Figure 7a). In contrast, DPCA, which involves targeted band selection, performed poorly, failing to enhance hematite signals across most of the study area, except for a few isolated pixels (Figure 7b).

For kaolinite, both PCA and DPCA were effective in delineating kaolinite-rich zones with high accuracy, showing strong agreement with the actual extent of the deposit. Notably, DPCA provided sharper boundary definition of the kaolinite zones (Figure 7c and Figure 7d).

Regarding calcite, PCA showed weak performance, producing spatially scattered and unreliable outputs (Figure 7e). However, DPCA (using bands 8 and 9) achieved more effective identification, with spatial distributions that aligned well with field data (Figure 7f). This highlights the advantage of selective band combinations in enhancing calcite detection via DPCA.

Evaluation of BRCC

The BRCC method, which incorporates targeted band ratios into RGB channels, provided highly interpretable visual outputs and successfully distinguished clay layers (particularly kaolinite) from carbonate units (Figure 8d). This success can be attributed to the deliberate design of the band ratios (e.g., b4/b6 for clay minerals, Figure 8b), which enhances spectral contrast.

Although ferric minerals were not strongly highlighted using this method (Figure 8c), the limited areas that were mapped corresponded to iron-rich pisolitic features. This partial overlap confirms the method's potential to detect hematite occurrences in specific geochemical contexts.

Evaluation of Machine Learning Approaches (RF and SVM)

The application of supervised machine learning algorithms, specifically RF and SVM, enabled the systematic classification and spatial delineation of kaolinite, hematite, calcite, and background units within the Semirom kaolin deposit. The RF model produced an overall accuracy of 69.13% with a Kappa coefficient of 0.546 (Table 7), while the SVM model achieved improved performance with an overall accuracy of 77.18% and a Kappa coefficient of 0.671 (Table 8). These metrics indicate a moderate to substantial agreement between the predicted classifications and the reference field and laboratory data.

Spatial analysis of the RF-derived mineral map (Figure 9) revealed that kaolinite occurrences were primarily associated with the red clay horizon, which is extensively exposed due to prior mining activities. Hematite pixels, co-located within the same red clay layer, caused partial spectral interference, which is reflected in the lower accuracy for kaolinite classification (User Accuracy = 56.25%; Producer Accuracy = 29.03%). In contrast, SVM (Figure 10), benefiting from its capacity to model complex, non-linear relationships in high-dimensional feature space, provided improved discrimination between kaolinite and hematite, as reflected in higher user and producer accuracies (User Accuracy = 80.95%; Producer Accuracy = 54.84% for kaolinite).

Calcite classification was relatively stable across both algorithms, reflecting the distinct spectral signature of carbonate units in the SWIR and VNIR bands of ASTER. Background areas were also reliably identified, though minor commission errors occurred, primarily due to mixed pixels along unit boundaries.

The observed classification errors are predominantly attributed to spectral overlap between kaolinite and hematite within the red clay layer. During mining operations, the red clay horizon acts as the basal layer beneath pure kaolin units and becomes the dominant exposed surface. The spectral contributions from both kaolinite and iron oxides result in mixed pixels, leading to partial misclassification. This phenomenon underscores the importance of integrating field-based reference data and considering lithological context when applying machine learning to hyperspectral or multispectral datasets.

Overall, the combination of RF and SVM provides complementary insights. While RF captures the general distribution patterns effectively, SVM offers enhanced precision in discriminating mineral phases with overlapping spectral characteristics. These findings demonstrate the potential of supervised machine learning for mineral mapping in complex sedimentary and lateritic environments, particularly when conventional spectral methods encounter limitations due to surface exposure and mineralogical mixtures.

Final Evaluation and Explanation of Methodological Successes and Failures

Field surveys and XRD analyses confirm the presence of the three primary minerals (kaolinite, hematite, and calcite) throughout the study area (Figure 13 & Figure 14). Therefore, the inability of certain remote sensing techniques to fully detect these minerals cannot be attributed to their absence, but rather to complex spectral interactions, surface modifications, and exposure conditions. Key factors influencing methodological limitations include:

Mixed spectral signatures. This effect contributes to misclassification in both RF and SVM, particularly in areas where kaolinite and iron oxides are closely interspersed.

Surface coverage and erosion**:** Secondary deposits and erosional processes obscure carbonate and other lithological units, reducing the detectability of underlying minerals.

Extraction and surface alteration**:** Mining activities have removed upper layers, exposing basal red clay horizons that dominate the spectral response, potentially masking pure kaolinite layers beneath.

Algorithm-specific limitations**:** While supervised machine learning approaches such as RF and SVM are robust, they remain sensitive to mixed pixels and overlapping spectral features, which can lower producer and user accuracies in complex mineralogical contexts.

These factors collectively explain why certain zones were only partially or ambiguously classified, despite the confirmed presence of the target minerals.

General insights on method performance and limitations

The evaluation of remote sensing and machine learning approaches highlights the complementary strengths and limitations of each technique. For kaolinite, KLI, PCA, DPCA, and BRCC effectively delineated kaolinite-rich zones. Machine learning, particularly SVM, further enhanced classification accuracy by distinguishing kaolinite from co-occurring hematite within the red clay horizon. RF captured general distribution patterns, while SVM offered higher precision in areas with spectral overlap. In the case of hematite, no single method fully captured its spatial extent. RF and BR provided partial but interpretable results, primarily in iron-rich pisolitic zones. SVM improved discrimination from kaolinite, although misclassifications persisted where both minerals co-occur. Regarding calcite, DPCA (bands 8 and 9) outperformed other methods in spatial coherence and alignment with field observations, followed by CLI and RBD, which achieved moderate success. Both RF and SVM reliably mapped calcite, with minor errors along unit boundaries due to mixed pixels. Persisting challenges include spectral overlap, surface cover disturbances, and the sensitivity of supervised algorithms to mixed pixels. Integrating multiple methods, considering geological context, and using accurate reference data are crucial for reliable mineral mapping in complex sedimentary and lateritic environments.

Although the incorporation of terrestrial spectral measurements acquired by a field spectrometer could potentially refine the spectral calibration and enhance the precision of mineral discrimination, such data were not obtainable in this study due to restricted accessibility of the instrument and the project's limited technical and financial resources. Nevertheless, the integration of ASTER multispectral data with comprehensive field validation and XRD confirmation yielded robust and consistent results, demonstrating the practical effectiveness of ASTER data for reconnaissance-scale mineral mapping.

Conclusion

This study assessed the applicability of ASTER satellite imagery combined with advanced image processing and machine learning techniques for mapping kaolinite, hematite, and calcite within the Semirom kaolin deposit, situated in the Zagros fold-and-thrust belt. A comprehensive workflow including BR, RBD, Spectral Indices, PCA, DPCA, BRCC, and supervised machine learning algorithms (RF and SVM) was implemented on preprocessed data, and validation was carried out through field observations and XRD analyses.

The results indicate that while no single approach provided universal accuracy, KLI, PCA, and DPCA were the most consistent in delineating kaolinite-rich zones. Machine learning, particularly SVM, improved discrimination between kaolinite and co-occurring hematite in the red clay horizon, while RF effectively captured general mineral distribution patterns. For calcite, DPCA using targeted SWIR bands achieved the highest spatial coherence, with RF and SVM also providing reliable mapping. Hematite, due to spectral overlap with clay minerals, was partially identified by RF and BR, and SVM enhanced its distinction from kaolinite in mixed pixels.

The main limitations arose from spectral interference between minerals, surface cover due to erosion, and the presence of mixed pixels affecting supervised algorithms. Despite these challenges, the integrated application of ASTER data, advanced processing methods, and machine learning proved effective for early-stage mineral exploration in complex tectonic settings. These methodologies not only allow precise identification of industrial minerals such as kaolinite, hematite, and calcite, but also have potential applicability in exploring both metallic and non-metallic deposits in other regions. Furthermore, considering the stratigraphic association between kaolinitic horizons at the Ilam–Sarvak formation boundary and known bauxite occurrences in the Zagros, the present findings offer valuable insights for future bauxite exploration.

Acknowledgements

The authors gratefully acknowledge Semirom Refractory Mining Company for funding the project and providing extensive support throughout the research and preparation of this manuscript.

Conflicts of interest

Reza Khaledi conducted the field investigations, collected the data, performed the remote sensing image processing, GIS analyses, spatial data processing, and map preparation, and was responsible for the development of the methodology, formal analyses, interpretation of results, visualization, and preparation of the original manuscript draft. Shojaeddin Niroomand contributed to the conceptualization of the study, supervised the research process, provided scientific guidance in the development and validation of the methodology, participated in the interpretation of the results, and critically reviewed and edited the manuscript. Abdorrahman Rajabi contributed to the conceptualization of the study, provided scientific consultation and supervision, participated in the validation and interpretation of the results, and critically reviewed and edited the manuscript.

Conflict of Interest

The authors declare that they have no known competing financial interests, personal relationships, or other circumstances that could have appeared to influence the work reported in this paper.

References

Abdelkareem, M., Abdalla, F., & Yousef, S. (2024). The use of ASTER and landsat remote sensing data for exploring hydrothermal mineral in Arabian-Nubian Shield. Kuwait Journal of Science, 51(3), 100240. https://doi.org/10.1016/j.kjs.2024.100240

Abrams, M. J., Rothery, D. A., & Pontual, A. (1988). Mapping in the Oman ophiolite using enhanced Landsat Thematic Mapper images. Tectonophysics, 151(1–4), 387–401.

https://doi.org/10.1016/0040-1951(88)90254-5
Ahmadnejad, F., & Mongelli, G. (2023). Geochemistry of Upper Cretaceous bauxite deposits, Zagros Fold Thrust Belt, SW Iran: Paleoenvironment and provenance constraints. Sedimentary Geology, 454, 106461. https://doi.org/10.1016/J.SEDGEO.2023.106461
Ahmadnejad, F., & Rafat, G. (2025). Geochemistry and genesis of rare earth minerals in the Tange Pirzal karstic bauxite deposit, Zagros Folded Belt, SW (Iran). Iranian Journal of Crystallography and Mineralogy, 30(3), 397–414. https://doi.org/10.52547/IJCM.30.3.397
Ahmadnejad, F., Zamanian, H., Taghipour, B., Zarasvandi, A., Buccione, R., & Salamab Ellahi, S. (2017). Mineralogical and geochemical evolution of the Bidgol bauxite deposit, Zagros Mountain Belt, Iran: Implications for ore genesis, rare earth elements fractionation and parental affinity. Ore Geology Reviews, 86, 755–783. https://doi.org/10.1016/J.OREGEOREV.2017.04.006
Alarifi, S. S., Abdelkareem, M., Abdalla, F., Abdelsadek, I. S., Gahlan, H., Al-Saleh, A. M., & Alotaibi, M. (2022). Fusion of Multispectral Remote-Sensing Data through GIS-Based Overlay Method for Revealing Potential Areas of Hydrothermal Mineral Resources. Minerals, 12(12). https://doi.org/10.3390/min12121577
Alavi, M., Navai, I., Yousefi, M., Sedaghat, M., & Hamzepour, B. (1996). Geological map of the Broojen Quadrangle, scale 1:250,000. Geological Survey of Iran.
Arjmandzadeh, R., Alirezaei, S., & Almasi, A. (2022). Tectonomagmatic reconstruction of the Upper Mesozoic-Cenozoic Neotethyan arcs in the Lut block, East Iran: a review and synthesis. Turkish Journal of Earth Sciences, 31(6), 520–544. https://doi.org/10.55730/1300-0985.1818
Arjmandzadeh, R., Karimpour, M. H., Mazaheri, S. A., Santos, J. F., Medina, J. M., & Homam, S. M. (2011). Sr–Nd isotope geochemistry and petrogenesis of the Chah-Shaljami granitoids (Lut Block, Eastern Iran). Journal of Asian Earth Sciences, 41(3), 283–296. https://doi.org/10.1016/J.JSEAES.2011.02.014
Bahrami, H., Esmaeili, P., Homayouni, S., Pour, A. B., Chokmani, K., & Bahroudi, A. (2024). Machine Learning-Based Lithological Mapping from ASTER Remote-Sensing Imagery. Minerals 2024, Vol. 14, Page 202, 14(2), 202. https://doi.org/10.3390/MIN14020202
Bahrami, H., Homayouni, S., McNairn, H., Hosseini, M., & Mahdianpari, M. (2022). Regional Crop Characterization Using Multi-Temporal Optical and Synthetic Aperture Radar Earth Observations Data. Canadian Journal of Remote Sensing, 48(2), 258–277. https://doi.org/10.1080/07038992.2021.2011180
Berberian, M. (1976). Contribution to the Seismotectonics of Iran (Part II). Geological Survey of Iran, Report No. 39, Tehran, Iran, 518 p.
Berberian, M., & King, G. C. P. (1981). TOWARDS A PALEOGEOGRAPHY AND TECTONIC EVOLUTION OF IRAN. Canadian Journal of Earth Sciences, 18(2), 210–265. https://doi.org/10.1139/e81-019
Breiman, L. (2001). Random forests. Machine Learning, 45(1), 5–32. https://doi.org/10.1023/A:1010933404324/METRICS
Canbaz, O., & Karaman, M. (2024). Geochemical characteristics and mapping of Reşadiye (Tokat-Türkiye) bentonite deposits using machine learning and sub-pixel mixture algorithms. Geochemistry, 84(4), 126123. https://doi.org/10.1016/J.CHEMER.2024.126123
Comby, O., Lambert, C., & Coajou, A. (1977). An Approach to the Structural Studies of the Zagros Fold Belt in the EGOCO Agreement Area. In Proceedings of the Second Geological Symposium of Iran, Tehran, Iran, pp. 103–159.
Cortes, C., & Vapnik, V. (1995). Support-vector networks. Machine Learning 1995 20:3, 20(3), 273–297. https://doi.org/10.1007/BF00994018
Crosta, A. P., & M. Moore, J. (1998). Enhancement of Landsat Thematic Mapper imagery for residual soil mapping in SW Minas Gerais state Brazil: a prospecting case history in Greenstone belt terrain. Proceedings of the 7th (ERIM) Thematic Conference: Remote Sensing for Exploration Geology, Calgary(2-6 Oct), 1173–1187. https://www.researchgate.net/publication/284966233_Enhancement_of_Landsat_Thematic_Mapper_imagery_for_residual_soil_mapping_in_SW_Minais_Gerais_State_Brazil_A_prospecting_case_history_in_Greenstone_belt_terrain
Dangeti, P. (2017). Statistics for Machine Learning: Techniques for Exploring Supervised, Unsupervised, and Reinforcement Learning Models with Python and R. Packt Publishing,

Birmingham, UK.
Ece, Ö. I., & Ercan, H. Ü. (2024). Global Occurrence, Geology and Characteristics of Hydrothermal-Origin Kaolin Deposits. Minerals 2024, Vol. 14, Page 353, 14(4), 353. https://doi.org/10.3390/MIN14040353
Esmaeilzadeh, N., Gani, N. D., Pour, A. B., Safari, M., & Fam, H. J. A. (2023). Hydrothermal Alteration and Lithological Mapping Using Landsat-9 and Aster Remote Sensing Spectral Imagery in the Northeast Mojave Desert, California. International Geoscience and Remote Sensing Symposium (IGARSS), 2023-July, 1972–1975. https://doi.org/10.1109/IGARSS52108.2023.10282311
Gaffey, S. J. (1986). Spectral reflectance of carbonate minerals in the visible and near infrared (0.35-2.55 microns): calcite, aragonite, and dolomite. American Mineralogist, 71(1), 151–162. https://www.scopus.com/record/display.uri?eid=2-s2.0-0022439742&origin=inward
Gallatin, K., & Albon, C. (2023). Machine Learning with Python Cookbook: Practical Solutions from Preprocessing to Deep Learning (2nd ed.). O'Reilly Media, Sebastopol, CA, USA, 413 p.
Habashi, J., Oskouei, M. M., & Moghadam, H. J. (2024). Classification of ASTER Data by Neural Network to Mapping Alterations Related to Copper and Iron Mineralization in Birjand. Journal of Mining and Environment, 15(2), 649–665. https://doi.org/10.22044/JME.2023.13640.2520
Hajaj, S., El Harti, A., Pour, A. B., Jellouli, A., Adiri, Z., & Hashim, M. (2024). A review on hyperspectral imagery application for lithological mapping and mineral prospecting: Machine learning techniques and future prospects. Remote Sensing Applications: Society and Environment, 35, 101218. https://doi.org/10.1016/J.RSASE.2024.101218
Hewson, R. D., Cudahy, T. J., Mizuhiko, S., Ueda, K., & Mauger, A. J. (2005). Seamless geological map generation using ASTER in the Broken Hill-Curnamona province of Australia. Remote Sensing of Environment, 99(1–2), 159–172. https://doi.org/10.1016/J.RSE.2005.04.025
Hunt, G. R. (1977). SPECTRAL SIGNATURES OF PARTICULATE MINERALS IN THE VISIBLE AND NEAR INFRARED. Geophysics, 42(3), 501–513. https://doi.org/10.1190/1.1440721
Huo, H., Ni, Z., Jiang, X., Zhou, P., & Liu, L. (2014). Mineral Mapping and Ore Prospecting with HyMap Data over Eastern Tien Shan, Xinjiang Uyghur Autonomous Region. Remote Sensing 2014, Vol. 6, Pages 11829-11851, 6(12), 11829–11851. https://doi.org/10.3390/RS61211829
Islam, N. U., Zhang, Q., Qiu, W., Liu, L., Khalil, Y. S., Ahmad, S. M., & Ahmad, W. (2024). Mineralogical mapping and lithological discrimination by using ASTER remote sensing data in the Chitral region, Khyber Pakhtunkhwa, Northern Pakistan. Earth Science Informatics, 17(6), 6075–6094. https://doi.org/10.1007/S12145-024-01483-4/METRICS
Iwasaki, A., & Tonooka, H. (2005). Validation of a crosstalk correction algorithm for ASTER/SWIR. IEEE Transactions on Geoscience and Remote Sensing, 43(12), 2747–2751. https://doi.org/10.1109/TGRS.2005.855066
Jain, R. (2022). Feature-Oriented Principal Component Selection (FPCS) for Delineation of the Geological Units Using the Integration of SWIR and TIR ASTER Data. In Recent Remote Sensing Sensor Applications - Satellites and Unmanned Aerial Vehicles (UAVs). IntechOpen. https://doi.org/10.5772/intechopen.99046
Jain, R., & Bhu, H. (2024). Potentials of spaceborne imaging spectrometer PRISMA, ASTER, and ALOS-1 PALSAR datasets for mineral mapping and geological controls of mineral deposit in Jahazpur, Rajasthan, India. Remote Sensing Applications: Society and Environment, 34, 101193. https://doi.org/10.1016/J.RSASE.2024.101193
Jain, R., Bhu, H., Kumar, H., & Purohit, R. (2022). Integration of multi-sensor remote sensing, geological and geochemical data for delineation of Pb–Zn bearing carbonates of Middle Aravalli group in Zawar–Dungarpur Belt, NW India. Geocarto International, 37(27), 17165–17199. https://doi.org/10.1080/10106049.2022.2123958;WGROUP:STRING:PUBLICATION
Kalinowski, A., & Oliver, S. (2004). ASTER Mineral Index Processing Manual. Remote Sensing Applications, Geoscience Australia, Internal Report, 39 pp.. http://www.ga.gov.au/image_cache/GA7833.pdf
Kaufmann, H. (1988). Mineral exploration along the aqaba-levant structure by use of tm- data concepts, processing and results. International Journal of Remote Sensing, 9(10–11), 1639–1658. https://doi.org/10.1080/01431168808954966
Khaledi, R. (2022). Geology, Mineralogy, Geochemistry and RS investigations of Semirom Kaolinite Deposit, Isfahan, M.Sc. Thesis, University of Tehran, Tehran, Iran.

Madani, A. A., & Emam, A. A. (2011). SWIR ASTER band ratios for lithological mapping and mineral exploration: a case study from El Hudi area, southeastern desert, Egypt. Arabian Journal of Geosciences, 4(1), 45–52. https://doi.org/10.1007/S12517-009-0059-8

Mars, J. C., & Rowan, L. C. (2011). ASTER spectral analysis and lithologic mapping of the Khanneshin carbonatite volcano, Afghanistan. Geosphere, 7(1), 276–289. https://doi.org/10.1130/GES00630.1

Mohamed, M. T. A. M., Al-Naimi, L. S., Mgbeojedo, T. I., & Agoha, C. C. (2021). Geological mapping and mineral prospectivity using remote sensing and GIS in parts of Hamissana, Northeast Sudan. Journal of Petroleum Exploration and Production, 11(3), 1123–1138. https://doi.org/10.1007/s13202-021-01115-3

Mountrakis, G., Im, J., & Ogole, C. (2011). Support vector machines in remote sensing: A review. ISPRS Journal of Photogrammetry and Remote Sensing, 66(3), 247–259. https://doi.org/10.1016/J.ISPRSJPRS.2010.11.001

Ninomiya, Y. (2003). Advanced Remote Lithologic Mapping in Ophiolite Zone with ASTER Multispectral Thermal Infrared Data. International Geoscience and Remote Sensing Symposium (IGARSS), 3, 1561–1563. https://doi.org/10.1109/igarss.2003.1294175

Ninomiya, Y., Fu, B., & Cudahy, T. J. (2005). Detecting lithology with Advanced Spaceborne Thermal Emission and Reflection Radiometer (ASTER) multispectral thermal infrared "radiance-at-sensor" data. Remote Sensing of Environment, 99(1–2), 127–139. https://doi.org/10.1016/j.rse.2005.06.009

Pattinson, R., & Takin, M. (1971). Geological Significance of Dezful Embayment Boundaries. Iranian Oil Operating Companies (IOOC), Report No. 1166 (Unpublished Report).

Rajendran, S. . (2009). Hyperspectral Remote Sensing and Spectral Signature Applications. In Hyperspectral Remote Sensing and Spectral Signature Applications. New India Publishing Agency. https://doi.org/10.59317/9789389992809

Rajendran, S., Hersi, O. S., Al-Harthy, A., Al-Wardi, M., El-Ghali, M. A., & Al-Abri, A. H. (2011). Capability of advanced spaceborne thermal emission and reflection radiometer (ASTER) on discrimination of carbonates and associated rocks and mineral identification of eastern mountain region (Saih Hatat window) of Sultanate of Oman. Carbonates and Evaporites, 26(4), 351–364. https://doi.org/10.1007/s13146-011-0071-4

Rajendran, S., & Nasir, S. (2017). Characterization of ASTER spectral bands for mapping of alteration zones of volcanogenic massive sulphide deposits. Ore Geology Reviews, 88, 317–335. https://doi.org/10.1016/j.oregeorev.2017.04.016

Rani, N., Mandla, V. R., & Singh, T. (2017). Evaluation of atmospheric corrections on hyperspectral data with special reference to mineral mapping. Geoscience Frontiers, 8(4), 797–808. https://doi.org/10.1016/J.GSF.2016.06.004

Reyment, R. A., & Davis, J. C. (1988). Statistics and Data Analysis in Geology. In Biometrics (Vol. 44, Issue 3). https://doi.org/10.2307/2531613

Richards, J. P., Spell, T., Rameh, E., Razique, A., & Fletcher, T. (2012). High Sr/Y Magmas Reflect Arc Maturity, High Magmatic Water Content, and Porphyry Cu ± Mo ± Au Potential: Examples from the Tethyan Arcs of Central and Eastern Iran and Western Pakistan. Economic Geology, 107(2), 295–332. https://doi.org/10.2113/ECONGEO.107.2.295

Rowan, L. C., & Mars, J. C. (2003). Lithologic mapping in the Mountain Pass, California area using Advanced Spaceborne Thermal Emission and Reflection Radiometer (ASTER) data. Remote Sensing of Environment, 84(3), 350–366. https://doi.org/10.1016/S0034-4257(02)00127-X

Salamab-Ellahi, S., Taghipour, B., & Mongelli, G. (2019). Clayey bauxite from the Irano-Himalayan belt: Critical metals, provenance and palaeoclimate in the Upper Cretaceous Semirom ore deposit, Zagros Mountain, Iran. Journal of Asian Earth Sciences, 172, 126–142. https://doi.org/10.1016/j.jseaes.2018.09.001

Salehi, S., Olsen, S. D., Pedersen, C. B., & Thorning, L. (2019). ASTER Data Analysis Applied to Mineral and Geological Mapping in North East Greenland: Documentation of the NEG ASTER Project. GEUS (Geological Survey of Denmark and Greenland), Danmarks og Grønlands Geologiske Undersøgelse Rapport 2019/7, Copenhagen, Denmark. https://doi.org/10.22008/gpub/32607

Sedaghat, M., & Gharib, F. (1999). Geological quadrangle map of Dena, scale 1:100,000. Geological Survey of Ira.

Sekandari, M., Masoumi, I., Pour, A. B., Muslim, A. M., Hossain, M. S., & Misra, A. (2022). ASTER and WorldView-3 satellite data for mapping lithology and alteration minerals associated with Pb-Zn

mineralization. Geocarto International, 37(6), 1782–1812. https://doi.org/10.1080/10106049.2020.1790676;REQUESTEDJOURNAL:JOURNAL:TGEI20;CTYPE:STRING:JOURNAL
Sengar, V. K., Venkatesh, A. S., Champati ray, P. K., Sahoo, P. R., Khan, I., & Chattoraj, S. L. (2020). Spaceborne mapping of hydrothermal alteration zones associated with the Mundiyawas-Khera copper deposit, Rajasthan, India, using SWIR bands of ASTER: Implications for exploration targeting. Ore Geology Reviews, 118, 103327. https://doi.org/10.1016/J.OREGEOREV.2020.103327
Shebl, A., Abdellatif, M., Badawi, M., Dawoud, M., Fahil, A. S., & Csámer, Á. (2023). Towards better delineation of hydrothermal alterations via multi-sensor remote sensing and airborne geophysical data. Scientific Reports, 13(1), 1–27.
Shuai, S., Zhang, Z., Lv, X., & Hao, L. (2022). Assessment of new spectral indices and multi-seasonal ASTER data for gypsum mapping. Carbonates and Evaporites, 37(2), 1–19. https://doi.org/10.1007/S13146-022-00775-4/FIGURES/4
Sikakwe, G. U. (2023). Mineral exploration employing drones, contemporary geological satellite remote sensing and geographical information system (GIS) procedures: A review. In Remote Sensing Applications: Society and Environment (Vol. 31, p. 100988). Elsevier. https://doi.org/10.1016/j.rsase.2023.100988
Story, M., & Congalton, R. G. (1983). Accuracy Assessment: A User'sPerspective. Photogrammetric Engineering and Remote Sensing. https://scholars.unh.edu/faculty_pubs/1247
Taghipour, B., Jahangirzadeh, S., & Mondillo, N. (2024). The mineralogy and geochemistry of the Pirashkaft bauxite, Zagros belt, Iran: New inferences on the paleo-climate at the time of formation and on the nature of the parent rock. Journal of Geochemical Exploration, 259, 107394. https://doi.org/10.1016/J.GEXPLO.2024.107394
Tende, H. M. ;, Abdel-Rahman, A. M. W. ;, Ene, A. M. ;, Awad, A. ;, Fahmy, H. A. ;, El-Awny, W. ;, Zakaly, H. M. H. ;, Hydrothermal, H. M. H., El-Desoky, H. M., Tende, A. W., Abdel-Rahman, A. M. W. ;, Ene, A. M. ;, Awad, H. A., Fahmy, W., El-Awny, H., & Zakaly, H. M. H. ; (2022). Hydrothermal Alteration Mapping Using Landsat 8 and ASTER Data and Geochemical Characteristics of Precambrian Rocks in the Egyptian Shield: A Case Study from Abu Ghalaga, Southeastern Desert, Egypt. Remote Sensing 2022, Vol. 14, Page 3456, 14(14), 3456. https://doi.org/10.3390/RS14143456
Thurmond, A. K., Abdelsalam, M. G., & Thurmond, J. B. (2006). Optical-radar-DEM remote sensing data integration for geological mapping in the Afar Depression, Ethiopia. Journal of African Earth Sciences, 44(2), 119–134. https://doi.org/10.1016/J.JAFREARSCI.2005.10.006
USGS. (2022). Advanced Spaceborne Thermal Emission and Reflection Radiometer (ASTER) Level 1 Precision Terrain Corrected Registered At-Sensor Radiance Product (AST_L1T). https://lpdaac.usgs.gov/documents/647/AST__L1T_User_Guide_V3.pdf
van der Meer, F. (1994). Sequential indicator conditional simulation and indicator kriging applied to discrimination of dolomitization in GER 63-channel imaging spectrometer data. Nonrenewable Resources, 3(2), 146–164. https://doi.org/10.1007/BF02286439
Xu, Y., Lin, Q., Shao, Y., & Wang, L. (2004). Extraction mechanism of alteration zones using ASTER imagery. International Geoscience and Remote Sensing Symposium (IGARSS), 6, 4174–4175. https://doi.org/10.1109/igarss.2004.1370054
Yan, J., Zhou, K., Liu, D., Wang, J., Wang, L., & Liu, H. (2014). Alteration information extraction using improved relative absorption band-depth images, from HJ-1A HSI data: a case study in Xinjiang Hatu gold ore district. International Journal of Remote Sensing, 35(18), 6728–6741. https://doi.org/10.1080/01431161.2014.963896;PAGE:STRING:ARTICLE/CHAPTER
Zamanian, H., Ahmadnejad, F., & Zarasvandi, A. (2016). Mineralogical and geochemical investigations of the Mombi bauxite deposit, Zagros Mountains, Iran. Chemie Der Erde, 76(1), 13–37. https://doi.org/10.1016/j.chemer.2015.10.001